



Exploring the nexus among roughness function, apparent slip velocity and upscaling coefficients for turbulence over porous/textured walls

Essam Nabil Ahmed¹  and Alessandro Bottaro¹ 

¹DICCA, Università degli Studi di Genova, via Montallegro 1, 16145 Genova, Italy

Corresponding author: Alessandro Bottaro, alessandro.bottaro@unige.it

(Received 29 April 2024; revised 4 January 2025; accepted 5 January 2025)

The interaction between a turbulent flow and a porous boundary is analysed with focus on the sensitivity of the roughness function, ΔU^+ , to the upscaled coefficients characterizing the wall. The study is aimed at (i) demonstrating that imposing effective velocity boundary conditions at a virtual plane boundary, next to the physical one, can efficiently simplify the direct numerical simulations (DNS); and (ii) pursuing correlations to estimate ΔU^+ *a priori*, once the upscaled coefficients are calculated. The homogenization approach employed incorporates near-interface advection via an Oseen-like linearization, and the macroscopic coefficients thus depend on both the microstructural details of the wall and a slip-velocity-based Reynolds number, Re_{slip} . A set of homogenization-simplified DNS is run to study the channel flow over transversely isotropic porous beds, testing values of the grains' pitch within $0 < \ell^+ < 40$. Reduction of the skin-friction drag is attainable exclusively over streamwise-aligned inclusions for ℓ^+ values up to 20–30. The drag increase over spanwise-aligned inclusions (or streamwise-aligned ones at large ℓ^+) is accompanied by enhanced turbulence levels, including intensified sweep and ejection events. The root-mean-square of the transpiration velocity fluctuations at the virtual plane, \tilde{V}_{rms} , is the key control parameter of ΔU^+ ; our analysis shows that, provided $\tilde{V}_{rms} \lesssim 0.25$, then \tilde{V}_{rms} is strongly correlated to a single macroscopic quantity, Ψ , which comprises the Navier-slip and interface/intrinsic permeability coefficients. Fitting relationships for ΔU^+ are proposed, and their applicability is confirmed against reference results for the turbulent flow over impermeable walls roughened with three-dimensional protrusions or different geometries of riblets.

Key words: turbulence simulation, turbulent boundary layers, homogenisation theory, porous/free-fluid dividing surface

1. Introduction

Turbulent channel flows are characterized by substantially large skin-friction drag, compared with laminar ones, and this can have severe consequences on the performance of fluid transport systems, in terms of efficiency, running costs and the reduction of emissions. There is a vast literature on turbulence in smooth channels (Kim *et al.* 1987; Mansour *et al.* 1988; Bernard *et al.* 1993; Jeong *et al.* 1997; Jiménez & Pinelli 1999; Vreman & Kuerten 2014), which has focused, for instance, on the behaviours of the primary turbulent fluctuations and the higher-order statistics, on the role of ejection and sweep events in the generation of Reynolds stresses, on nonlinear recurrent patterns, or on the autonomous regeneration cycle responsible for maintaining near-wall turbulence. Since the seminal work by Nikuradse (1933), the study of turbulent flow in channels delimited by rough boundaries has become a major focus of research, whether the goal is (i) to explore how given surface topographies can alter the near-wall turbulence and the skin-friction drag (Orlandi *et al.* 2006; Orlandi & Leonardi 2006, 2008; Wang *et al.* 2021; Monti *et al.* 2022; Hao & García-Mayoral 2025), (ii) to propose and test simplified models for numerical analysis (Bottaro 2019; Lācis *et al.* 2020; Ahmed *et al.* 2022*b*) or even predictive correlations (Forooghi *et al.* 2017; Flack *et al.* 2020) or (iii) to optimize and assess the feasibility of wall-based energy-saving control strategies of either active (Antonia *et al.* 1995; Kang & Choi 2000; Choi 2002; Wise & Ricco 2014; Cheng *et al.* 2021) or passive nature (Walsh & Lindemann 1984; Bechert *et al.* 1997; Rastegari & Akhavan 2015; Rosti *et al.* 2018; Endrikat *et al.* 2021*b*). This introductory section centres around these important aspects.

Passive drag reduction techniques (i.e. microtextured surfaces, permeable substrates, etc. enable, with no energy input, to favourably manipulate the turbulent boundary layer with a view to reducing the turbulent skin-friction drag compared with the smooth surface case) have been the subject of intense research activities. Properly designed superhydrophobic surfaces and liquid-infused surfaces, permitting large effective slip thanks to air (or liquid lubricant, respectively) being trapped within grooves/cavities/microgrates formed on them, can yield substantial drag reduction in turbulent channel flows (Park *et al.* 2013; Rastegari & Akhavan 2015; Fu *et al.* 2017; Chang *et al.* 2019). Riblets (longitudinal surface grooves) have proved to mitigate the velocity fluctuations near the wall, resulting in a more uniform flow field (Bechert & Bartenwerfer 1989). The skin-friction drag over surfaces altered with riblets is crucially sensitive to their geometry and to the Reynolds number of the flow in their vicinity (characterized, for instance, by the lateral spacing of riblets measured in wall units, ℓ^+) as found by many investigators (Walsh & Lindemann 1984; Bechert *et al.* 1997; El-Samni *et al.* 2007; Gatti *et al.* 2020; Endrikat *et al.* 2021*a,b*; von Deyn *et al.* 2022). For example, the experiments by Bechert *et al.* (1997) on different configurations of riblets revealed that an optimized drag reduction of almost 10% can be attained, in particular with longitudinal blade ribs having depth and thickness equal to, respectively, 0.5 and 0.02 times the lateral rib spacing and with $\ell^+ \approx 17$. It should be noted that drag reduction ceases when ℓ^+ exceeds a value of approximately 30, and this is associated with the occurrence of inertial-flow mechanisms such as a Kelvin–Helmholtz instability (García-Mayoral & Jimenez 2011*b*; Endrikat *et al.* 2021*a*). Manipulating the turbulent boundary layer and achieving skin-friction reduction by means of properly engineered permeable substrates has recently caught the attention of many researchers. The porous medium permeability coefficients (\hat{K}_{ij}) and the Navier slip lengths ($\hat{\lambda}_i$) are the main parameters whose role has been examined in a number of investigations, with different

microstructures of the substrate, sizes of the solid inclusions, porosities (θ) and flow conditions. Throughout this paper, \hat{x} , \hat{y} and \hat{z} refer to, respectively, the streamwise, wall-normal and spanwise directions. Among the configurations studied, transversely isotropic porous beds of streamwise-preferential permeability $\hat{K}_{xx} \gg \hat{K}_{yy} = \hat{K}_{zz}$, for instance those constructed with cylindrical inclusions elongated in the direction of the mean flow, are repeatedly reported to potentially reduce drag in turbulent channel flows; the underpinning of their function, analogous to that of riblets, has been explained by Abderrahaman-Elena & García-Mayoral (2017), Gómez-de-Segura *et al.* (2018a), Gómez-de-Segura & García-Mayoral (2019) and Chavarin *et al.* (2021). These authors have found that, at relatively large values of the wall-normal permeability, Kelvin–Helmholtz-like rollers are generated near the porous–free-fluid interface, and this adversely affects the drag-reducing mechanism. Streamwise-preferential porous substrates characterized by relatively large $\sqrt{\mathcal{K}_{yy}^+}$ (considerably beyond the threshold identified by Gómez-de-Segura & García-Mayoral (2019) for the emergence of Kelvin–Helmholtz vortices) were considered, among other configurations, in the scale-resolving direct numerical simulations (DNS) by Khorasani *et al.* (2024) and the experiments by Vijay & Luhar (2024), and drag increase was confirmed. For a complete picture, it is also useful to cite the experiments by Morimoto *et al.* (2024) where drag either remained unchanged or was found to increase (with respect to smooth wall) for the case of streamwise-preferential permeable beds under conditions that were expected, on the basis of the numerical findings in Gómez-de-Segura & García-Mayoral (2019), to yield drag reduction instead. Morimoto *et al.* (2024) commented that it is difficult in practice (unlike in numerical work) to maintain the large uniform porosity and streamwise permeability when the substrate/channel interface is approached, and this adversely affects slippage. Several other studies of turbulence over porous substrates were conducted. Among the most relevant ones, we cite those conducted by Suga’s group (Suga *et al.* 2013, 2018; Suga 2016; Kuwata & Suga 2017), and those by Breugem *et al.* (2006), Manes *et al.* (2011), Rosti *et al.* (2015, 2018), Wang *et al.* (2021, 2022), Esteban *et al.* (2022) and Hao & García-Mayoral (2025).

Investigating how the microscale features of the surface (e.g. roughness, porosity, superhydrophobicity, etc.) can alter the characteristics of the turbulent motion above it, and thus skin-friction drag or heat/mass transfer effectiveness, is important in several applications for both predictive and optimization purposes. The numerical complexity and the high computational cost associated with resolving turbulent fields near and across surface microdetails represent a challenge, because of the large variety of surface topographies encountered in practice, the computational costs required to carry out well-resolved DNS or large-eddy simulations of the motion, and the uncertainties/errors related with the numerical representation of the rough surface or of the grain shape and distributions for the case of a porous bed. Despite the recent computational advances which have permitted numerical investigations with unprecedented levels of accuracy (Chung *et al.* 2021), the aforementioned factors represent a major hurdle when the optimization of the surface is the ultimate goal. In this respect, characterizing surfaces by key parameters available *a priori* and exhibiting a strong relation with the roughness function, for example, can be very beneficial. However, this is a complex undertaking, and the quantities widely investigated throughout the literature are, in principle, available only *a posteriori* (i.e. after conducting the numerical/experimental study of the turbulent flow over the surface) and, hence, of limited use for prediction purposes. For example, we mention here (i) the equivalent sand-grain size, k_s , first introduced by Schlichting (1937) and later used as a classifier for rough surfaces in a large body of studies (refer to the limitations and drawbacks highlighted by Jiménez (2004) and

Abderrahaman-Elena *et al.* (2019)); and (ii) the virtual origins of mean flow and turbulence (Luchini *et al.* 1991; Jiménez 1994; Luchini 1996), with successive efforts devoted, in recent years, to the exploration of the statistical quantities whose near-wall behaviour defines the virtual origin of turbulence (Gómez-de-Segura *et al.* 2018*b*; Abderrahaman-Elena *et al.* 2019; Bernardini *et al.* 2021; Ibrahim *et al.* 2021; Khorasani *et al.* 2022; Wong *et al.* 2024). On the positive side, predictive models based on the aforementioned concepts, albeit not yet generalized, are beginning to emerge (Flack & Schultz 2010; Yang & Meneveau 2016; Yang *et al.* 2016; Forooghi *et al.* 2017; Flack *et al.* 2020; Khorasani *et al.* 2022). It is also worth referring to the recent work on machine-learning-based predictive methods by, for example, Jouybari *et al.* (2021), Lee *et al.* (2022), Yang *et al.* (2023, 2024) and Shi *et al.* (2024).

The development of accurate macroscopic models for the fluid–wall interaction has become a very active field of research in the last decade or so. These are viable tools capable of simplifying the numerical analysis while maintaining an acceptable level of accuracy. The asymptotic, multiscale homogenization theory (Babuska 1976; Mei & Vernescu 2010) is a theoretical framework through which the rapidly varying properties characterizing a heterogeneous surface (irregular, rough, lubricant-infused or porous, *inter alia*) can be replaced by homogeneous upscaled quantities such as the Navier’s slip lengths or the interface permeability coefficients (Jiménez Bolaños & Vernescu 2017; Lācis *et al.* 2017; Bottaro 2019; Zampogna *et al.* 2019*a*; Lācis *et al.* 2020). The latter are necessary for the formulation of effective boundary conditions, free of empirical parameters, to be imposed at a fictitious plane interface next to the physical textured boundary; the macroscale behaviour of the channel flow is then studied numerically, eschewing the numerical resolution of flow details between/in close vicinity of the solid protrusions/grains and, consequently, alleviating mesh requirements and computational costs. The validity of the asymptotic homogenization approach is contingent on the presence of well-separated scales, for instance a microscopic length scale ($\tilde{\ell}$) related to the surface texture and a macroscopic one ($\mathcal{L} \gg \tilde{\ell}$) related to the large-scale flow structures in the channel, such that we are able to define the small parameter $\epsilon = \tilde{\ell}/\mathcal{L} \ll 1$ and seek a solution of the problem up to the required order of accuracy in terms of ϵ . Jiménez Bolaños & Vernescu (2017) provided a robust homogenization-based method for the evaluation of the slip coefficient, contributing to the classical order-one slip condition over a textured surface, first proposed by Navier (1823) on the basis of empirical considerations. High-order effective boundary conditions were derived by Bottaro & Naqvi (2020) and Ahmed *et al.* (2022*a*) for the flow over a rough surface and by Lācis *et al.* (2020), Sudhakar *et al.* (2021), Naqvi & Bottaro (2021) and Ahmed *et al.* (2022*b*) for the flow over a porous bed. Definitions of the three velocity components at the fictitious interface, valid up to second order in ϵ , are now available; this is crucial under turbulent flow conditions since turbulent fluctuations along directions both tangent and normal to the fictitious interface considerably affect the behaviour of the turbulent boundary layer and, therefore, the skin-friction drag (Orlandi *et al.* 2006; Orlandi & Leonardi 2006, 2008; Bottaro 2019; Lācis *et al.* 2020). The near-wall advection was incorporated into the analysis by means of an Oseen’s approximation in the studies by Buda (2021) and Ahmed & Bottaro (2024), and this permitted to widen considerably the applicability range of the model.

The present work is aimed at investigating the hydrodynamic interaction between a porous/rough boundary and a fluid under turbulent conditions, with the aid of a homogenization framework. The main focus is on exploring the relationship between the roughness function ΔU^+ (i.e. the shift in the intercept of the logarithmic velocity profile) and the macroscopic coefficients (i.e. the Navier-slip coefficients and the

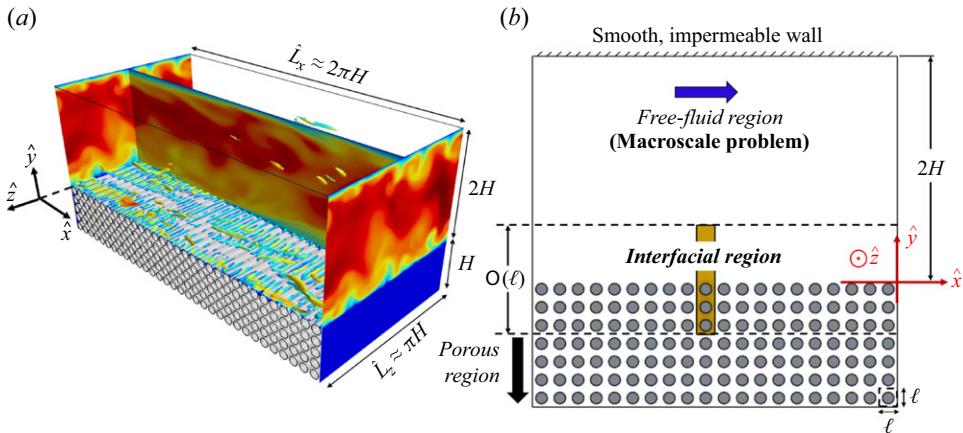


Figure 1. (a) Sketch of the full domain for the case of a channel delimited from the top by a smooth, impermeable wall and from the bottom by a porous bed formed by spanwise-elongated cylindrical grains. Panel (b) illustrates in a constant \hat{z} -section the decomposition of the domain into three distinct subregions; the brown volume represents the horizontally periodic elementary cell of the microscopic problem.

interface/intrinsic permeabilities) contributing to the effective boundary conditions at the wall. Throughout the work, it is assumed that the roughness elements do not protrude significantly into the free-fluid turbulent region, for outer layer similarity to hold (Townsend 1976). The study is twofold. First, turbulent channel flows over permeable boundaries of different geometries are considered, and high-order effective boundary conditions of the three velocity components, defined at a fictitious plane boundary tangent to the grains, are formulated (§ 2), validated (§ 3.1) and employed to simplify a set of DNS (§ 3.2); the mean velocity profiles are obtained and the main turbulence statistics near the porous–free-fluid interface are analysed to interpret the drag-reducing/increasing effects of the porous patterns. Second, in order to estimate the roughness function *a priori*, without the need for running DNS, the available results are fitted to generate an explicit expression linking ΔU^+ to the upscaled coefficients of interest (§ 3.3); the generality of the fitting correlation(s) is confirmed via validation against results from the literature for the turbulent flow over rough, impermeable walls (§ 3.4). A discussion on the applicability range of the model is provided in § 4, and general conclusions are given in § 5.

2. Problem statement and upscaling approach

2.1. Governing equations and domain decomposition

Let us consider the turbulent flow of a viscous, incompressible, Newtonian fluid in a channel delimited from one side (at $\hat{y} = 2H$) by a smooth, impermeable wall and from the other side (at $\hat{y} \leq 0$) by a permeable substrate constructed with spanwise-elongated (\hat{z} -aligned) solid inclusions, regularly arranged with given periodicity ℓ in the streamwise and wall-normal directions (\hat{x} and \hat{y} , respectively), see figure 1. The velocity components ($\hat{u}_1 = \hat{u}$, $\hat{u}_2 = \hat{v}$, $\hat{u}_3 = \hat{w}$) and the pressure \hat{p} are the dependent variables, to be evaluated over space ($\hat{x}_1 = \hat{x}$, $\hat{x}_2 = \hat{y}$, $\hat{x}_3 = \hat{z}$) and time \hat{t} . The conservation equations governing the flow can be expressed as follows:

$$\frac{\partial \hat{u}_i}{\partial \hat{x}_i} = 0, \quad \rho \left(\frac{\partial \hat{u}_i}{\partial \hat{t}} + \hat{u}_j \frac{\partial \hat{u}_i}{\partial \hat{x}_j} \right) = -\frac{\partial \hat{p}}{\partial \hat{x}_i} + \mu \frac{\partial^2 \hat{u}_i}{\partial \hat{x}_j^2}, \quad (2.1)$$

with ρ and μ the fluid density and dynamic viscosity, respectively.

We identify two characteristic length scales: a microscopic one, $\tilde{\ell}$, characterizing the porous bed, and a macroscopic one, \mathcal{L} , related to the large-scale motion in the channel. Provided that the two length scales are well-separated, i.e. $\tilde{\ell} \ll \mathcal{L}$, it is possible to manipulate the microscale problem by means of an asymptotic analysis in terms of a small parameter $\epsilon = \tilde{\ell}/\mathcal{L} \ll 1$. As illustrated in figure 1, the flow domain is decomposed into three distinct subdomains: a channel-flow region away from the porous–free-fluid interface (superscript ‘C’), an interfacial region (superscript ‘I’) and a region within the porous layer away from boundaries, governed by Darcy’s law (superscript ‘P’). Correspondingly, the following three sets of normalized variables are proposed:

$$X_i = \frac{\hat{x}_i}{\mathcal{L}}, \quad U_i^C = \frac{\hat{u}}{\mathcal{U}}, \quad P^C = \frac{\hat{p}}{\rho\mathcal{U}^2}, \tag{2.2a}$$

$$x_i = \frac{\hat{x}_i}{\tilde{\ell}}, \quad U_i^I = \frac{\hat{u}}{\epsilon\mathcal{U}}, \quad P^I = \frac{\hat{p}}{\mu\mathcal{U}/\mathcal{L}}, \tag{2.2b}$$

$$x_i = \frac{\hat{x}_i}{\tilde{\ell}}, \quad U_i^P = \frac{\hat{u}}{\epsilon^2\mathcal{U}}, \quad P^P = \frac{\hat{p}}{\mu\mathcal{U}/\mathcal{L}}, \tag{2.2c}$$

where \mathcal{U} is a suitable macroscopic velocity scale; a discussion on the proper selection of scales is provided later. Based on the normalization above, the governing (2.1) can be recast into the following dimensionless forms in the \bullet^C , \bullet^I and \bullet^P regions, respectively:

$$\frac{\partial U_i^C}{\partial X_i} = 0, \quad \frac{\partial U_i^C}{\partial t} + U_j^C \frac{\partial U_i^C}{\partial X_j} = -\frac{\partial P^C}{\partial X_i} + \frac{1}{Re} \frac{\partial^2 U_i^C}{\partial X_j^2}, \tag{2.3a}$$

$$\frac{\partial U_i^I}{\partial x_i} = 0, \quad \epsilon^2 Re \left(\frac{\partial U_i^I}{\partial t} + U_j^I \frac{\partial U_i^I}{\partial x_j} \right) = -\frac{\partial P^I}{\partial x_i} + \frac{\partial^2 U_i^I}{\partial x_j^2}, \tag{2.3b}$$

$$\epsilon \frac{\partial U_i^P}{\partial x_i} = 0, \quad \epsilon^4 Re U_j^P \frac{\partial U_i^P}{\partial x_j} = -\frac{\partial P^P}{\partial x_i} + \epsilon \frac{\partial^2 U_i^P}{\partial x_j^2}, \tag{2.3c}$$

with $Re = \rho\mathcal{U}\mathcal{L}/\mu$. Note that the time scale is the same in the interface and free-fluid region ($t = \hat{t}\mathcal{U}/\mathcal{L}$) and that in the bulk of the porous domain the motion is assumed steady. In the intermediate and porous regions, the dependent variables are function of both the fast (microscopic) and the slow (macroscopic) coordinates (x_i, X_i , respectively), whilst in the channel-flow region, the dependent variables vary spatially with the macroscopic coordinates, X_i , only. A fictitious dividing surface between the channel-flow region and the interfacial layer is defined at $\hat{x}_2 = \hat{y}_\infty$, and continuity of the velocity and the traction vectors is applied there. With $y_\infty = \hat{y}_\infty/\tilde{\ell}$ and $\mathcal{Y}_\infty = \hat{y}_\infty/\mathcal{L} = \epsilon y_\infty$ the microscopic and the macroscopic vertical coordinates of this interface, respectively, the matching conditions can be written as follows:

$$\lim_{x_2 \rightarrow y_\infty} U_i^I = \frac{1}{\epsilon} \lim_{X_2 \rightarrow \mathcal{Y}_\infty} U_i^C, \tag{2.4a}$$

$$\lim_{x_2 \rightarrow y_\infty} \left(-P^I \delta_{i2} + \frac{\partial V^I}{\partial x_i} + \frac{\partial U_i^I}{\partial y} \right) = \lim_{X_2 \rightarrow \mathcal{Y}_\infty} \left(-Re P^C \delta_{i2} + \frac{\partial V^C}{\partial X_i} + \frac{\partial U_i^C}{\partial Y} \right), \tag{2.4b}$$

with δ_{ij} the Kronecker index. For the conditions above to be valid, y_∞ must be sufficiently large such that the \bullet^I variables become uniform in x and z at the virtual interface.

2.2. Asymptotic analysis of the microscale problem

The dependent variables in the interfacial and the porous subdomains are expanded in terms of ϵ as

$$U_i^{\mathcal{I}} = U_i^{\mathcal{I}(0)} + \epsilon U_i^{\mathcal{I}(1)} + \epsilon^2 U_i^{\mathcal{I}(2)} + \dots, \quad P^{\mathcal{I}} = P^{\mathcal{I}(0)} + \epsilon P^{\mathcal{I}(1)} + \epsilon^2 P^{\mathcal{I}(2)} + \dots, \tag{2.5}$$

$$U_i^{\mathcal{P}} = U_i^{\mathcal{P}(0)} + \epsilon U_i^{\mathcal{P}(1)} + \epsilon^2 U_i^{\mathcal{P}(2)} + \dots, \quad P^{\mathcal{P}} = P^{\mathcal{P}(0)} + \epsilon P^{\mathcal{P}(1)} + \epsilon^2 P^{\mathcal{P}(2)} + \dots \tag{2.6}$$

Furthermore, the gradients are recast using the chain rule $(\partial/\partial x_i) \rightarrow (\partial/\partial x_i) + \epsilon (\partial/\partial X_i)$. The asymptotic expressions are substituted into the equations governing the flow in the microscopic regions, for the microscale problems to be reconstructed at different orders of ϵ . It has been shown (Naqvi & Bottaro 2021) that the resulting systems of equations for the interfacial and the porous regions can be combined by defining a composite description of the asymptotic expansions, that is

$$u_i = u_i^{(0)} + \epsilon u_i^{(1)} + \mathcal{O}(\epsilon^2), \quad p = p^{(0)} + \epsilon p^{(1)} + \mathcal{O}(\epsilon^2), \tag{2.7a}$$

with

$$u_i^{(0)} = \begin{cases} U_i^{\mathcal{I}(0)}, & y \in \mathcal{I} \\ \epsilon U_i^{\mathcal{P}(0)}, & y \in \mathcal{P} \end{cases}, \quad u_i^{(1)} = \begin{cases} U_i^{\mathcal{I}(1)}, & y \in \mathcal{I} \\ \epsilon U_i^{\mathcal{P}(1)}, & y \in \mathcal{P} \end{cases}, \tag{2.7b}$$

and

$$p^{(0)} = \begin{cases} P^{\mathcal{I}(0)}, & y \in \mathcal{I} \\ P^{\mathcal{P}(0)} + \epsilon P^{\mathcal{P}(1)}, & y \in \mathcal{P} \end{cases}, \quad p^{(1)} = \begin{cases} P^{\mathcal{I}(1)}, & y \in \mathcal{I} \\ \epsilon P^{\mathcal{P}(2)}, & y \in \mathcal{P} \end{cases}. \tag{2.7c}$$

The following composite system, valid over the whole region below the dividing interface (i.e. $x_2 < y_\infty$), is thus obtained:

$$\begin{cases} \partial_i u_i = -\epsilon \partial'_i u_i^{(0)} + \mathcal{O}(\epsilon^2) \\ -\partial_i p + \partial_j^2 u_i = \mathcal{R} u_j \partial_j u_i + \epsilon \left[\partial'_i p^{(0)} - 2\partial_j \partial'_j u_i^{(0)} + \mathcal{R} u_j^{(0)} \partial'_j u_i^{(0)} \right] + \mathcal{O}(\epsilon^2) \end{cases} \tag{2.8}$$

with $\mathcal{R} = \epsilon^2 Re$ a microscopic Reynolds number and with derivatives indicated by $\partial_i = (\partial/\partial x_i)$ and $\partial'_i = (\partial/\partial X_i)$.

In order to treat the problem above, we first simplify it by linearizing the convective terms applying an Oseen approximation. In particular, a constant value is assigned to the streamwise velocity component, u_1 , near the interface, chosen as the surface-averaged slip velocity $u_{slip} = (\hat{u}_{slip}/\epsilon\mathcal{U})$ (with \hat{u}_{slip} the dimensional slip velocity at the plane $\hat{y} = 0$), i.e. $u_j^{(0)} \simeq (u_{slip}, 0, 0)$ (other choices are clearly possible). For example, Bottaro (2019) tested the friction velocity as advective speed; results shown in the following support the present choice of the slip velocity). Thus, the advection term in (2.8) simplifies as $\mathcal{R} u_{slip} \partial_1 u_i$, with

$$\mathcal{R} u_{slip} = \frac{\rho \hat{u}_{slip} \tilde{\ell}}{\mu} = Re_{slip}. \tag{2.9}$$

The quantity Re_{slip} is a slip-velocity Reynolds number, based on the microscopic length scale $\tilde{\ell}$; as we will see later, its value is not necessarily small. The composite system (2.8)

is now approximated as

$$\begin{cases} \partial_i u_i = -\epsilon \partial'_i u_i^{(0)} + \mathcal{O}(\epsilon^2) \\ -\partial_i p + \partial_j^2 u_i = Re_{slip} \partial_1 u_i + \epsilon \left[\partial'_i p^{(0)} - 2\partial_j \partial'_j u_i^{(0)} + Re_{slip} \partial'_1 u_i^{(0)} \right] + \mathcal{O}(\epsilon^2) \end{cases} \quad (2.10)$$

The leading-order problem reads

$$\mathcal{O}(1) : \begin{cases} \partial_i u_i^{(0)} = 0, \\ -\partial_i p^{(0)} + \partial_j^2 u_i^{(0)} = Re_{slip} \partial_1 u_i^{(0)}, \\ \left(-p^{(0)} \delta_{i2} + \partial_2 u_i^{(0)} + \partial_i u_2^{(0)} \right)_{x_2=y_\infty} = S_{i2}^C, \end{cases} \quad (2.11)$$

with S_{i2}^C the macroscopic traction vector evaluated at $X_2 = \mathcal{Y}_\infty$, i.e.

$$S_{i2}^C = \boldsymbol{\sigma}^C \cdot \mathbf{e}_2|_{x_2=y_\infty} = \left(\frac{\partial U^C}{\partial Y} + \frac{\partial V^C}{\partial X}, -Re P^C + 2 \frac{\partial V^C}{\partial Y}, \frac{\partial W^C}{\partial Y} + \frac{\partial V^C}{\partial Z} \right) \Big|_{x_2=y_\infty}, \quad (2.12)$$

where $\boldsymbol{\sigma}^C$ is the stress tensor. From now on, the outer dependent variables are written without the superscript \bullet^C .

At next order, we have

$$\mathcal{O}(\epsilon) : \begin{cases} \partial_i u_i^{(1)} = -\partial'_i u_i^{(0)}, \\ -\partial_i p^{(1)} + \partial_j^2 u_i^{(1)} = Re_{slip} \left(\partial_1 u_i^{(1)} + \partial'_1 u_i^{(0)} \right) + \partial'_i p^{(0)} - 2\partial_j \partial'_j u_i^{(0)}, \\ \left(-p^{(1)} \delta_{i2} + \partial_2 u_i^{(1)} + \partial_i u_2^{(1)} \right)_{x_2=y_\infty} = - \left(\partial'_2 u_i^{(0)} + \partial'_i u_2^{(0)} \right)_{x_2=y_\infty}. \end{cases} \quad (2.13)$$

The linearity of (2.11) and (2.13) permits us to assume generic solutions of the problems. For the leading-order problem, we express the dependent variables as

$$\begin{cases} u_i^{(0)} = u_{ij}^\dagger S_{j2}, \\ p^{(0)} = p_j^\dagger S_{j2}, \end{cases} \quad (2.14)$$

with the closure variables, u_{ij}^\dagger and p_j^\dagger , dependent on only the microscopic coordinates, x_j . Decoupled *ad hoc* auxiliary systems arise from plugging the generic solutions into (2.11); they are

$$\begin{cases} \partial_i u_{ij}^\dagger = 0, \\ -\partial_i p_j^\dagger + \partial_l^2 u_{ij}^\dagger = Re_{slip} \partial_1 u_{ij}^\dagger, \\ \left(-p_j^\dagger \delta_{i2} + \partial_2 u_{ij}^\dagger + \partial_i u_{2j}^\dagger \right) \Big|_{x_2=y_\infty} = \delta_{ij}, \end{cases} \quad (2.15)$$

where the microscopic problems correspond to $j = 1, 2, 3$. For the problem forced by S_{22} (i.e. with $j = 2$), the analytical solution $u_{i2}^\dagger = 0$, $p_2^\dagger = -1$ is easily retrieved. At $O(\epsilon)$ the following generic forms hold:

$$\begin{cases} u_i^{(1)} = u_{ijk}^\dagger \partial'_k S_{j2}, \\ p^{(1)} = p_{jk}^\dagger \partial'_k S_{j2}, \end{cases} \quad (2.16)$$

leading to

$$\begin{cases} \partial_i u_{ijk}^\ddagger = -u_{kj}^\dagger, \\ Reslip \left(\partial_1 u_{ijk}^\ddagger + u_{ij}^\dagger \delta_{k1} \right) = -\partial_i p_{jk}^\ddagger - p_j^\dagger \delta_{ki} + \partial_l^2 u_{ijk}^\ddagger + 2\partial_k u_{ij}^\dagger, \\ \left(-p_{jk}^\ddagger \delta_{i2} + \partial_2 u_{ijk}^\ddagger + \partial_i u_{2jk}^\ddagger \right) \Big|_{x_2=y_\infty} = - \left(u_{ij}^\dagger \delta_{k2} + u_{2j}^\dagger \delta_{ik} \right) \Big|_{x_2=y_\infty}; \end{cases} \quad (2.17)$$

these are nine decoupled systems, i.e. corresponding to $j, k = 1, 2, 3$. The closure problems (2.15) and (2.17) are to be solved in a representative unit cell of the microscopic region, subject to periodicity of all the dependent variables along x and z and to the boundary conditions $u_{ij}^\dagger = 0$ and $u_{ijk}^\ddagger = 0$ on the solid grains, arising from the no-slip condition. Further, the microscopic unit cell is delimited from the bottom (theoretically at $y \rightarrow -\infty$) by the bulk of the porous domain, where dependent variables are cyclic of period 1 also along y ; from a numerical perspective, results do not change provided the domain is at least two rows deep.

2.3. Formal expressions of the effective boundary conditions

Numerical solutions are sought for systems (2.15) and (2.17), with focus on the values of the fields at $x_2 = y_\infty$ since $u_{ij}^\dagger|_{y_\infty}$ and $u_{ijk}^\ddagger|_{y_\infty}$ are eventually the coefficients needed to close the macroscopic effective boundary conditions for the velocity; these conditions result from matching the velocity vector at the fictitious interface between the channel-flow and the interfacial regions, as per (2.4a). The upscaled conditions, second-order accurate in terms of ϵ , are

$$U_i|_{y_\infty} = \epsilon \left(u_i^{(0)} \Big|_{y_\infty} + \epsilon u_i^{(1)} \Big|_{y_\infty} \right) + \mathcal{O}(\epsilon^3) = \epsilon u_{ij}^\dagger \Big|_{y_\infty} S_{j2} + \epsilon^2 u_{ijk}^\ddagger \Big|_{y_\infty} \frac{\partial S_{j2}}{\partial X_k} + \mathcal{O}(\epsilon^3). \quad (2.18)$$

The numerical procedure to solve the closure problems is similar to that followed by Naqvi & Bottaro (2021) and Ahmed *et al.* (2022b) for porous media of either isotropic (such as spherical grains) or transversely isotropic microstructures in the $\hat{x} - \hat{z}$ plane (such as spanwise- or streamwise-elongated elements). We focus on the same parameters that do not vanish at the matching interface found in these references,

$$\begin{aligned} u_{11}^\dagger \Big|_{y_\infty} &= y_\infty + \lambda_x, & u_{33}^\dagger \Big|_{y_\infty} &= y_\infty + \lambda_z, \\ -u_{211}^\ddagger \Big|_{y_\infty} &= u_{121}^\ddagger \Big|_{y_\infty} = 0.5 y_\infty^2 + \lambda_x y_\infty + \mathcal{K}_{xy}^{itf}, \\ -u_{233}^\ddagger \Big|_{y_\infty} &= u_{323}^\ddagger \Big|_{y_\infty} = 0.5 y_\infty^2 + \lambda_z y_\infty + \mathcal{K}_{zy}^{itf}, \\ u_{222}^\ddagger \Big|_{y_\infty} &= \mathcal{K}_{yy}, \end{aligned} \quad (2.19)$$

with λ_x and λ_z the dimensionless Navier’s slip coefficients in the streamwise and the spanwise directions, respectively, \mathcal{K}_{xy}^{itf} and \mathcal{K}_{zy}^{itf} the interface permeability coefficients and \mathcal{K}_{yy} an intrinsic permeability component. The novel contribution here is the incorporation of the effect of near-interface inertia on the microscale flow behaviour, which renders the aforementioned parameters sensitive to the value of $Reslip$.

Once relations (2.19) are plugged into (2.18) macroscopic matching conditions at the interface $Y_\infty = \epsilon y_\infty$ between the intermediate and the outer region are obtained.

These conditions can then be transferred to $Y = 0$ by a second-order Taylor expansion, to eventually yield the following effective boundary conditions:

$$U|_{Y=0} = \epsilon \lambda_x S_{12}|_{Y=0} + \epsilon^2 \mathcal{K}_{xy}^{itf} \frac{\partial S_{22}}{\partial X} \Big|_{Y=0} + \mathcal{O}(\epsilon^3), \quad (2.20a)$$

$$V|_{Y=0} = -\epsilon^2 \mathcal{K}_{xy}^{itf} \frac{\partial S_{12}}{\partial X} \Big|_{Y=0} - \epsilon^2 \mathcal{K}_{zy}^{itf} \frac{\partial S_{32}}{\partial Z} \Big|_{Y=0} + \epsilon^2 \mathcal{K}_{yy} \frac{\partial S_{22}}{\partial Y} \Big|_{Y=0} + \mathcal{O}(\epsilon^3), \quad (2.20b)$$

$$W|_{Y=0} = \epsilon \lambda_z S_{32}|_{Y=0} + \epsilon^2 \mathcal{K}_{zy}^{itf} \frac{\partial S_{22}}{\partial Z} \Big|_{Y=0} + \mathcal{O}(\epsilon^3). \quad (2.20c)$$

At this point, something should be said about the scales $(\tilde{\ell}, \mathcal{L}, \mathcal{U})$ used to normalize the preceding equations, and on whether the principle of separation of scales is satisfied. If the magnitude of the macroscopic pressure gradient driving the flow in the channel is $\mathcal{M} = \left| \Delta \hat{p} / \hat{L}_x \right|$, one may derive a stress $\tau_{\mathcal{M}} = \mathcal{M} H = (\tau_B + \tau_T)/2$, with τ_B and τ_T the total shear stresses at $Y = 0$ (bottom) and $Y = 2$ (top), respectively. The corresponding shear velocity $u_{\tau(\mathcal{M})} = \sqrt{\tau_{\mathcal{M}}/\rho}$ is chosen here as the macroscopic velocity scale, i.e. $\mathcal{U} = u_{\tau(\mathcal{M})}$. This is an appropriate characterization of the velocity of near-wall eddies, since it is known that the root-mean-square (r.m.s.) of the fluctuating speed scales with the friction velocity. As far as the macroscopic length scale is concerned, it has been proposed first by Luchini (1996) that the important boundary condition for turbulence is that experienced by quasistreamwise vortices. The relevant length scale should thus be the vortex diameter which is around 20 viscous units, i.e. $\mathcal{L} \sim \alpha (\nu u_{\tau(\mathcal{M})})$, with α a constant close to 20. As far as the microlength scale is concerned, we observe that in the asymptotic analysis by Saffman (1971) for the case of the flow over an isotropic porous substrate of permeability K , the choice $\tilde{\ell} = \sqrt{K}$ was made. Recently, Hao & García-Mayoral (2025) have argued that the effect of deep porous substrates (those considered in the present paper can also be characterized as ‘deep’) on the near-wall flow is essentially governed by the intrinsic permeability of the medium, which, in all cases considered here, is a small fraction of ℓ^2 (cf. also Mei & Vernescu (2010); Zampogna *et al.* (2019a); Lācis *et al.* (2020); Naqvi & Bottaro (2021); Sudhakar *et al.* (2021)), with ℓ the periodicity of the grains. For regularly roughened walls, when a substrate permeability cannot be defined, the proper length scale should be a measure of the slip length of the texture, also a small fraction of the periodicity, ℓ . At this point, we anticipate that ℓ^+ is approximately 20 times larger than $\sqrt{\mathcal{K}_{yy}^+}$ (this will be shown later for all porous substrates considered.) Thus, it seems appropriate to say that $\tilde{\ell} \sim \ell/\alpha$, with the same value of the constant α as in the definition of the macrolength \mathcal{L} . We are now able to estimate the small parameter ϵ of the expansion; it is found that $\epsilon \sim \ell^+/\alpha^2$ ranges from around 0.025 up to 0.1 for cylindrical inclusions having ℓ^+ values between 10 and 40. For the ‘modified’ grains described later, ϵ would be even smaller, considering that such inclusions tend to block the flow and the permeability is much lower than in the previous case.

On the basis of the arguments presented, microscopic and macroscopic length scales are sufficiently well separated, for all the cases treated in this paper. The microscopic length scale in our analysis is the displacement of the origin of the near-wall vortex, caused by the presence of either a rough or a porous substrate; the macroscopic scale is the diameter of the vortex itself. One referee of this work objected vigorously to our choice of microscopic length scale, arguing that the only proper microscale is the pattern periodicity. If, as they

objected, this were indeed the case, then $\tilde{\ell} \sim \ell$ and the parameter of the expansion would become $\epsilon \sim \ell^+/\alpha$, which exceeds 1 for $\ell^+ > 20$. Beyond $\ell^+ \approx 20$, they argued, separation of scale, and the expansion proposed, would be untenable. In the end, we believe that only *a posteriori* verifications against feature-resolving results can inform on the domain of validity of the upscaling procedure adopted; this crucial point will be addressed in §§ 3.1 and 4.

In dimensional form, the effective boundary conditions are the same that have been found before (Naqvi & Bottaro 2021) and read

$$\hat{u}|_0 \approx \hat{\lambda}_x \left(\frac{\partial \hat{u}}{\partial \hat{y}} + \frac{\partial \hat{v}}{\partial \hat{x}} \right) \Big|_0 + \frac{\hat{\mathcal{K}}_{xy}^{itf}}{\mu} \frac{\partial}{\partial \hat{x}} \left(-\hat{p} + 2\mu \frac{\partial \hat{v}}{\partial \hat{y}} \right) \Big|_0, \quad (2.21a)$$

$$\hat{v}|_0 \approx \frac{\hat{\mathcal{K}}_{yy}}{\mu} \frac{\partial}{\partial \hat{y}} \left(-\hat{p} + 2\mu \frac{\partial \hat{v}}{\partial \hat{y}} \right) \Big|_0 - \hat{\mathcal{K}}_{xy}^{itf} \frac{\partial}{\partial \hat{x}} \left(\frac{\partial \hat{u}}{\partial \hat{y}} + \frac{\partial \hat{v}}{\partial \hat{x}} \right) \Big|_0 - \hat{\mathcal{K}}_{zy}^{itf} \frac{\partial}{\partial \hat{z}} \left(\frac{\partial \hat{w}}{\partial \hat{y}} + \frac{\partial \hat{v}}{\partial \hat{z}} \right) \Big|_0, \quad (2.21b)$$

$$\hat{w}|_0 \approx \hat{\lambda}_z \left(\frac{\partial \hat{w}}{\partial \hat{y}} + \frac{\partial \hat{v}}{\partial \hat{z}} \right) \Big|_0 + \frac{\hat{\mathcal{K}}_{zy}^{itf}}{\mu} \frac{\partial}{\partial \hat{z}} \left(-\hat{p} + 2\mu \frac{\partial \hat{v}}{\partial \hat{y}} \right) \Big|_0. \quad (2.21c)$$

Further considerations, simplifications and implementation-related details concerning the condition (2.21b) are given in appendix A. After having established the effective conditions which hold at $\hat{y} = 0$, we can render them adimensional in the most convenient way. Thus, we now choose to scale the governing (2.1) for the free-fluid region, as well as the corresponding interface conditions (2.21a)–(2.21c), by the use of geometric scales (cf. figure 1); this corresponds to setting $\mathcal{L} = H$ in equations (2.2a–2.2c). By the same token, the microscopic problems in the unit cells is rescaled with the periodicity of the pattern and this amounts to setting $\tilde{\ell} = \ell$ in equations (2.2a–2.2c) so that, eventually, ϵ is defined by the ratio ℓ over H , like in the laminar case (Naqvi & Bottaro 2021; Ahmed & Bottaro 2024). Having rescaled the problem for computational convenience, the dimensional model coefficients now read

$$\hat{\lambda}_{x,z} = \lambda_{x,z} l, \quad \hat{\mathcal{K}}_{xy,zy}^{itf} = \mathcal{K}_{xy,zy}^{itf} l^2, \quad \hat{\mathcal{K}}_{yy} = \mathcal{K}_{yy} l^2. \quad (2.22)$$

We want to emphasize that these coefficients are not empirical, but arise from the solution of auxiliary systems of equations solved in the \hat{x} - or \hat{z} -periodic elementary cell of figure 1. The two terms, $\hat{\mathcal{K}}_{xy}^{itf}$ and $\hat{\mathcal{K}}_{zy}^{itf}$, are interface permeabilities since, by analogy to Darcy’s law in the bulk of the porous domain, they multiply the streamwise and spanwise gradients of the pressure in the expressions of $\hat{u}|_0$ and $\hat{w}|_0$. They differ from the corresponding intrinsic permeability components which come from the solution of Stokes problems in a triply periodic unit cell taken in the bulk of the porous region and, as such, have little in common with the flow around the porous–free-fluid interface (Bottaro 2019).

2.4. Evaluation of the macroscopic coefficients for selected geometries

Typical geometries of the inclusions used to construct the porous media under study are illustrated in figure 2; they are aligned in either the streamwise direction (substrates *LC* and *LM*) or the spanwise direction (substrates *TC* and *TM*), all satisfying a porosity $\theta = 0.5$, where θ is defined by considering a cubic unit cell within the porous region and evaluating the ratio of the volume occupied by the fluid to the total volume of the cell.

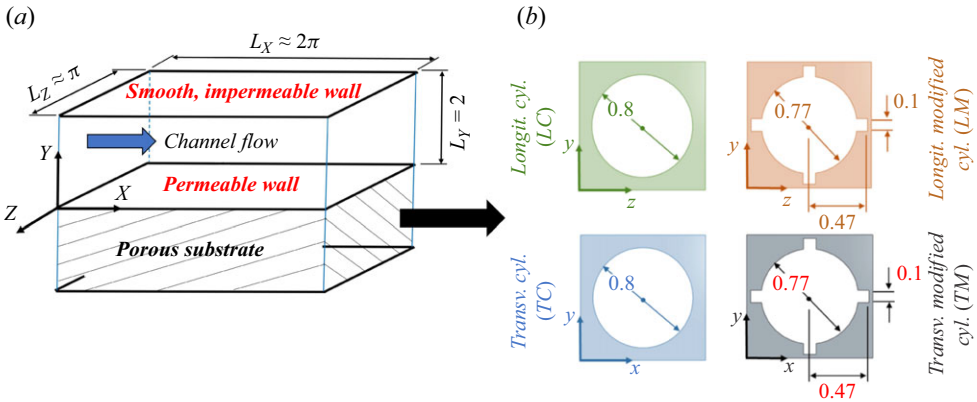


Figure 2. The problems under study. The computational domain is displayed in (a), with the dimensions indicated in the macroscopic coordinates (normalized by half the channel height). (b) The bulk unit cell of the different porous media considered are drawn in microscopic dimensionless coordinates. All media have porosity $\theta = 0.5$.

A simple method, similar to that followed by Ahmed *et al.* (2022b), is used to numerically evaluate the macroscopic coefficients in the effective boundary conditions. First, the systems governing the microscale fields u_{11}^\dagger and u_{33}^\dagger are solved on a microscopic domain with a sufficiently large value of y_∞ (like, for instance, the domain sketched in figure 3a). In this work, the solution of the closure problems is conducted using finite-volume discretization, as by the implementation of Simcenter STAR-CCM+ software; in general, the microscopic domain is discretized into polygonal/polyhedral cells with sufficient mesh refinement in close vicinity of the porous–free-fluid interface such that grid-independent results for the closure fields are eventually obtained. Second, the Navier’s slip coefficients (λ_x, λ_z) are estimated by averaging u_{11}^\dagger and u_{33}^\dagger , respectively, over the plane $y = 0$. The numerical values of the interface permeability coefficients can be computed via the following volume integrals:

$$\begin{aligned} \mathcal{K}_{xy}^{itf} &= \int_{\mathcal{V}_0} u_{11}^\dagger \, dV, \\ \mathcal{K}_{zy}^{itf} &= \int_{\mathcal{V}_0} u_{33}^\dagger \, dV, \end{aligned} \tag{2.23}$$

where \mathcal{V}_0 denotes the whole fluid’s volume in the elementary cell below the interface at $y = 0$. This renders the dimensionless Navier-slip and the interface permeability coefficients dependent, in general, on the geometry of the inclusions and the slip-velocity Reynolds number, Re_{slip} , which appears in the microscopic auxiliary systems (note that, after rescaling, Re_{slip} is now defined with ℓ as length scale).

On the other hand, the medium permeability \mathcal{K}_{yy} is intrinsic to the geometry of the porous region, where the velocity level is much smaller than u_{slip} and the inertial effects are thus negligible; \mathcal{K}_{yy} can be estimated by solving a Stokes system on a triply periodic cell of the porous domain, imposing unit forcing along y , and evaluating the superficial average of the corresponding microscopic field over that cell (Mei & Vernescu 2010).

Transverse (\hat{z} -elongated) and longitudinal (\hat{x} -elongated) inclusions allow for further simplification of the microscopic, auxiliary problems, by setting either $\partial/\partial x_3$ or $\partial/\partial x_1$ to zero, respectively, yielding two-dimensional systems of equations. For the case of spanwise-elongated inclusions, we get the following two systems of interest at leading order:

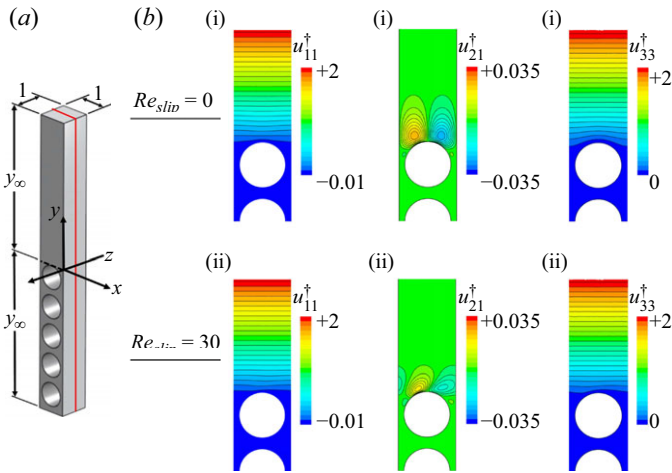


Figure 3. Contours of the microscopic variables u_{11}^\dagger , u_{21}^\dagger and u_{33}^\dagger at (i) $Re_{slip} = 0$ and (ii) $Re_{slip} = 30$, shown over an $x - y$ plane for the case of transverse cylinders of porosity $\theta = 0.5$. Close-ups of the contours near the fluid–porous interface are presented, while the typical domain considered in the simulations is shown in (a). Slip and permeability coefficients are independent of the value of y_∞ , provided it is larger than 2.

$$\begin{cases} \partial_1 u_{11}^\dagger + \partial_2 u_{21}^\dagger = 0, \\ -\partial_1 p_1^\dagger + \partial_1^2 u_{11}^\dagger + \partial_2^2 u_{11}^\dagger = Re_{slip} \partial_1 u_{11}^\dagger, \\ -\partial_2 p_1^\dagger + \partial_1^2 u_{21}^\dagger + \partial_2^2 u_{21}^\dagger = Re_{slip} \partial_1 u_{21}^\dagger, \\ \left(\partial_2 u_{11}^\dagger + \partial_1 u_{21}^\dagger \right) \Big|_{x_2=y_\infty} = 1, \\ \left(-p_1^\dagger + 2\partial_2 u_{21}^\dagger \right) \Big|_{x_2=y_\infty} = 0, \end{cases} \quad (2.24)$$

and

$$\begin{cases} \partial_1^2 u_{33}^\dagger + \partial_2^2 u_{33}^\dagger = Re_{slip} \partial_1 u_{33}^\dagger, \\ \left(\partial_2 u_{33}^\dagger \right) \Big|_{x_2=y_\infty} = 1. \end{cases} \quad (2.25)$$

The numerical solutions of the previous systems under Stokes conditions and at $Re_{slip} = 30$ are shown in figure 3 for the case of transverse cylindrical inclusions, while the dependence of the macroscopic coefficients on Re_{slip} is displayed in figure 4(a) for the substrates *TC* and *TM*. A preliminary estimation of the value of the slip velocity can be obtained from the first-order term in the effective boundary condition of U , equation (2.20a), which may be recast in terms of the wall distance in viscous units ($Y^+ = Y Re_{\tau(\mathcal{M})}$) and the mean velocity, already normalized by $u_{\tau(\mathcal{M})}$ and hence from now on indicated as \bar{U}^+ , as follows:

$$\bar{U}^+ \Big|_{Y=0} \approx \lambda_x^+ \frac{\partial \bar{U}^+}{\partial Y^+} \Big|_{Y=0}, \quad (2.26)$$

where $\lambda_x^+ = (\rho u_{\tau(\mathcal{M})} \hat{\lambda}_x / \mu) = \epsilon Re_{\tau(\mathcal{M})} \lambda_x$. Provided the roughness maintains a sufficiently small amplitude so that the velocity gradient $(\partial \bar{U}^+ / \partial Y^+) \Big|_{Y=0}$ at the virtual wall remains close to 1, (2.26) simplifies to a Dirichlet boundary condition, i.e.

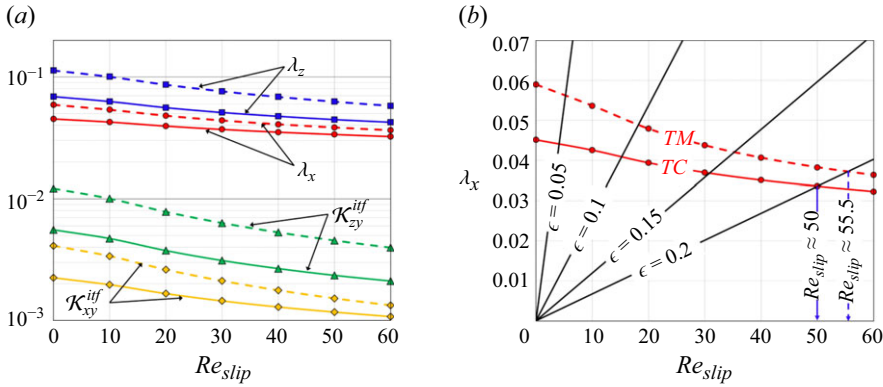


Figure 4. Behaviours of the homogenization model parameters. Panel (a) displays results of the closure problems for the Navier-slip and interface permeability coefficients as functions of Re_{slip} for the porous substrates *TC* (solid lines) and *TM* (dashed lines). In panel (b), the linear relation (2.28) between λ_x and Re_{slip} is plotted (black lines) for four values of ϵ , fixing $Re_{\tau(\mathcal{M})} = 193$, in order to evaluate Re_{slip} at the intersection points.

$$\overline{U} \Big|_{Y=0} = \frac{\hat{u}_{slip}}{u_{\tau(\mathcal{M})}} \approx \epsilon Re_{\tau(\mathcal{M})} \lambda_x, \tag{2.27}$$

which means that the slip-velocity Reynolds number can be written as

$$Re_{slip} = \frac{\rho \hat{u}_{slip} \ell}{\mu} = \frac{\rho u_{\tau(\mathcal{M})} \ell}{\mu} \epsilon Re_{\tau(\mathcal{M})} \lambda_x = \epsilon^2 Re_{\tau(\mathcal{M})}^2 \lambda_x. \tag{2.28}$$

With $\lambda_x = (Re_{slip}/\epsilon^2 Re_{\tau(\mathcal{M})}^2)$, a linear relation between λ_x and Re_{slip} can be drawn for different values of ϵ , at the fixed value of the friction Reynolds number, $Re_{\tau(\mathcal{M})} = 193$; cf. figure 4(b). The value of Re_{slip} at the intersection point is evaluated as shown in figure 4(b), yielding as an immediate consequence all the macroscopic coefficients at this value; table 1 reports all coefficients for ϵ ranging from 0.05 to 0.2. The reader is referred here to the work by Fairhall *et al.* (2019) where useful findings regarding the possible deviations of the slip lengths from the viscous predictions are presented for surface textures different from those considered here.

Streamwise-elongated inclusions (substrates *LC* and *LM*) represent a special case since inertial effects at the microscale level disappear as a consequence of setting $\partial/\partial x_1$ to 0 in the auxiliary systems (Luchini *et al.* 1991); as such, the macroscopic coefficients are independent of Re_{slip} . The coefficients for these substrates are directly available by revisiting the results for *TC* and *TM*, at $Re_{slip} = 0$, and simply switching the streamwise and spanwise coordinates.

3. The macroscale problems

For the DNS of the macroscale problem, considering the turbulent channel flow over different porous substrates, the numerical procedure is the same as that followed by Ahmed *et al.* (2022b). The dimensions of the computational domain, which represents here the free-fluid region above the modelled substrate, are $L_X \times L_Y \times L_Z = 2\pi \times 2 \times \pi$ (cf. figure 1) as adopted by other researchers before (Khorasani *et al.* 2022; Hao & García-Mayoral 2025). The mesh is uniform in the streamwise (*X*) and spanwise (*Z*) directions, while it is stretched gradually in the wall-normal direction (*Y*) departing from the upper and lower walls (thinnest layer) towards the centreline of the channel

Substrate	Re_{slip} (intersection)	Dimensionless macroscopic coefficients				
		λ_x	λ_z	\mathcal{K}_{xy}^{itf}	\mathcal{K}_{zy}^{itf}	\mathcal{K}_{yy}
TC_5	4.1	0.0440	0.0663	0.0021	0.0052	0.0018
TC_{10}	15.2	0.0409	0.0591	0.0018	0.0042	0.0018
TC_{15}	30.9	0.0368	0.0506	0.0014	0.0031	0.0018
TC_{20}	50.0	0.0336	0.0445	0.0012	0.0023	0.0018
LC_{5-20}	Any	0.0688	0.0451	0.0056	0.0022	0.0018
TM_5	5.3	0.0562	0.1062	0.0037	0.0110	0.00012
TM_{10}	18.2	0.0489	0.0888	0.0028	0.0082	0.00012
TM_{15}	35.3	0.0421	0.0721	0.0019	0.0058	0.00012
TM_{20}	55.5	0.0372	0.0599	0.0014	0.0042	0.00012
LM_{5-20}	Any	0.1130	0.0590	0.0121	0.0041	0.00012

Table 1. Values of the macroscopic coefficients for the 16 porous substrates considered in the present study. For all patterns, the porosity is $\theta = 0.5$ and $Re_{\tau(\mathcal{M})} = 193$, while $\epsilon = \ell/H$ is varied from 0.05 (subscript 5) to 0.2 (subscript 20).

(thickest layer); the grid spacings in viscous units are $h_x^+ = 9.47$, $h_z^+ = 6.32$, $h_y^+|_{min} = 0.27$, $h_y^+|_{max} = 9.25$. The simulations are run using the Simcenter STAR-CCM+ finite-volume-based software. For the convective fluxes, a hybrid third-order discretization scheme is employed, formulated as a linear blend between a MUSCL (monotone upstream-centred schemes for conservation laws) third-order upwind and a third-order central-differencing scheme, with the upwind blending factor set to 0.1 (i.e. 10% MUSCL and 90% central differencing); the reader is referred to the paper by van Leer & Nishikawa (2021) for further information on MUSCL, and to the work by West & Carraeni (2015) in which the hybrid MUSCL/CD approach is implemented. The computation of gradients is based on the least squares method, with the Venkatakrisnan gradient limiter activated (Venkatakrisnan 1993). A pressure correction approach is used for the pressure–velocity coupling; a second-order fully implicit scheme is employed for the temporal discretization with time step set to $0.0015 H/u_\tau$ and a minimum of 20 internal iterations performed for each time step. The averaging time, after the initial transient phase, is generally between 18 and 35 H/u_τ . With the above-mentioned settings and schemes, Ahmed *et al.* (2022b) found excellent agreement between the numerical results obtained for turbulence in a smooth channel (at $Re_\tau = 193$) and corresponding results from previous studies (Kim *et al.* 1987; Vreman & Kuerten 2014) (unfortunately, a direct comparison with other homogenization-based DNS is not possible, since no other paper we are aware of uses the same boundary conditions described here to model turbulence over a rough, permeable wall). Given that the DNS are run here for turbulence over different modelled substrates using a fixed time step ($0.0015 H/u_\tau$), there is a possibility that the maximum convective Courant–Friedrichs–Lewy number exceeds 1. This issue has been checked, and it has been found that the maximum convective Courant–Friedrichs–Lewy number increases to around 2 for the largest value of ϵ considered, i.e. $\epsilon = 0.2$, in the vicinity of the interface ($0 \lesssim Y^+ \lesssim 15$). Because of this, the homogenization–based direct simulation for the pattern TC_{20} was rerun with a smaller time step, satisfying $CFL \lesssim 1$; the comparison revealed marginal deviations in the results for the main quantities characterizing the turbulent flow. Finally, it is appropriate to provide further details on how the transpiration boundary condition (2.21b) is enforced in the numerical code; they are given in appendix A.

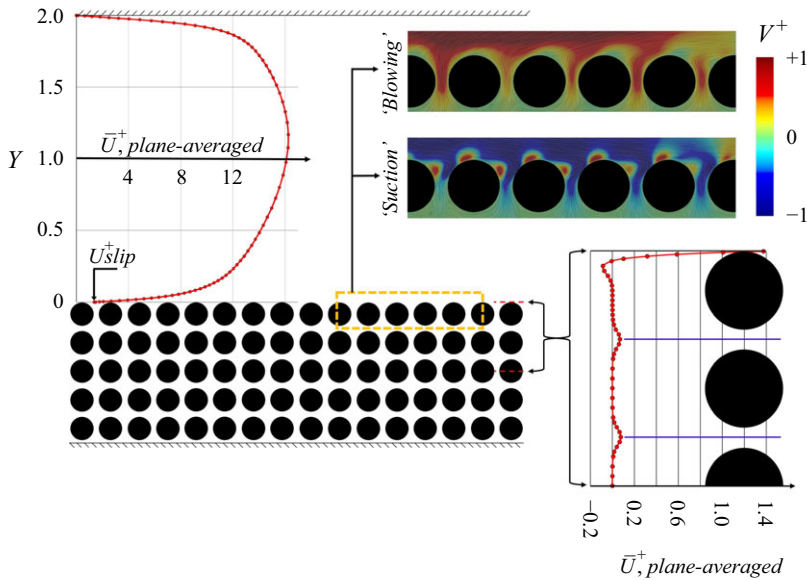


Figure 5. Full feature-resolving simulation of the coupled flow problem including the flow through and the turbulent flow over the porous substrate TC_{20} at $Re_{\tau(\mathcal{M})} = 193$: profiles of the X - Z -averaged mean velocity across the free-fluid region and closely below the fluid-porous interface are plotted. Instantaneous distributions (examples) of the interface-normal velocity component, V^+ , captured during ‘suction’ and ‘blowing’ events are also displayed.

3.1. Validation of the model

The applicability of the upscaling approach followed is assessed here by considering the turbulent flow ($Re_{\tau(\mathcal{M})} = 193$) in a channel delimited from the bottom ($Y \leq 0$) by the substrate TC_{20} (transverse cylinders, $\epsilon = 0.2$), and validating sample results of the homogenized simulation, based on the effective boundary conditions (2.20a–2.20c) with the macroscopic coefficients given in table 1, against a classical fine-grained simulation. The mesh requirements, and thus the numerical cost, of the latter are much higher since it needs to resolve the seepage flow in the bulk of the porous domain and to account for the interactions occurring across the interfacial region, where significant ejection and sweep events take place (cf. figure 5). Quantitatively, the number of finite-volume cells in the fully resolving DNS ($N_{cells} \approx 7.3 \times 10^6$) is four times that in the homogenized DNS ($N_{cells} \approx 1.8 \times 10^6$). Another point to be taken into account with respect to the full DNS is the technical complexity associated with the mesh generation, especially in the interfacial region. An unstructured grid was used in the porous substrate and in the lower-half of the channel; the cells are polygonal in section (on the $X - Y$ plane) and are extruded in the spanwise direction with a uniform spacing of ≈ 6 viscous units. For the top row of cylinders (the closest to the porous-free-fluid interface), the mesh is refined such that the first cell centre is at a distance of around 0.3 viscous units from the cylindrical grain, measured in the direction normal to the boundary.

The results in the free-fluid region are presented and compared (homogenization-based versus fine-grained) in figures 6 and 7, in terms of the following dimensionless parameters: the mean velocity, \bar{U}^+ ; the r.m.s. of the fluctuations in the velocity components, $(U_{rms}, V_{rms}, W_{rms}) = (\overline{U'U'}^{1/2}, \overline{V'V'}^{1/2}, \overline{W'W'}^{1/2})$ where the turbulent fluctuations are defined as $U'_i = U_i^+ - \bar{U}_i^+$; the intensity of the fluctuations, $(I_U, I_V, I_W) =$

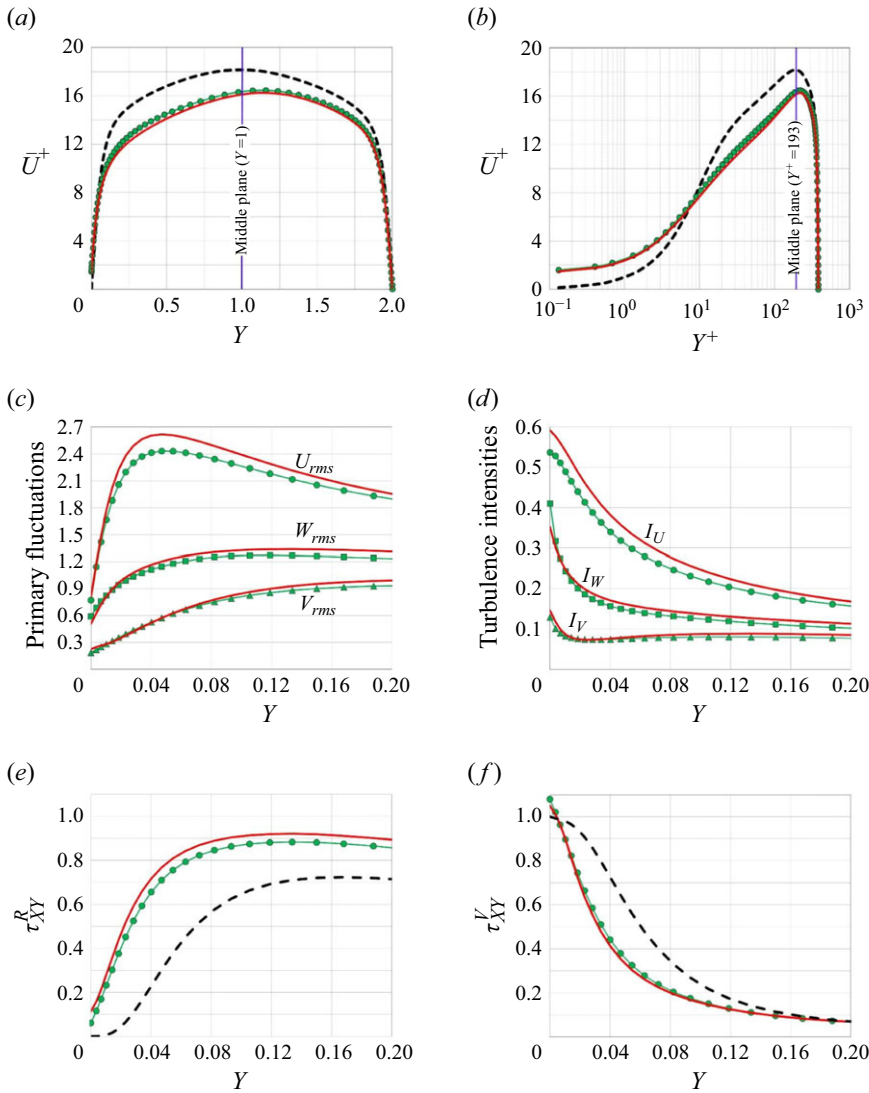


Figure 6. Turbulent channel flow ($Re_{\tau(\mathcal{M})} = 193$) over the porous substrate TC_{20} : predictions of the homogenized model, indicated by green lines with filled symbols, for (a,b) the mean velocity profile across the channel and for the near-interface distributions of (c) the r.m.s. of the turbulent fluctuations in the three velocity components, (d) the turbulence intensities and (e,f) the Reynolds/viscous shear stresses are validated against results of the full simulation (red lines). The dashed black profiles refer to the corresponding smooth, impermeable channel case.

$((U_{rms}/\bar{U}^+), (V_{rms}/\bar{U}^+), (W_{rms}/\bar{U}^+))$; the Reynolds shear stress, $\tau_{XY}^R = -\overline{U'V'}$; the viscous shear stress, $\tau_{XY}^V = (1/Re_{\tau(\mathcal{M})}) (\partial\bar{U}^+/\partial Y)$; and the production rate of the turbulent kinetic energy, $P_T = (-1/Re_{\tau(\mathcal{M})}) \overline{U'_i U'_j} (\partial\bar{U}_i^+/\partial X_j)$. While figure 6 focuses on the validation of the present model with the effective boundary conditions of the three velocity components imposed at $Y = 0$, figure 7 shows, in addition, the corresponding macroscopic results when the interface-normal velocity component is suppressed (i.e. $V|_{Y=0} = 0$) and only the in-plane slip velocities are applied; this is important

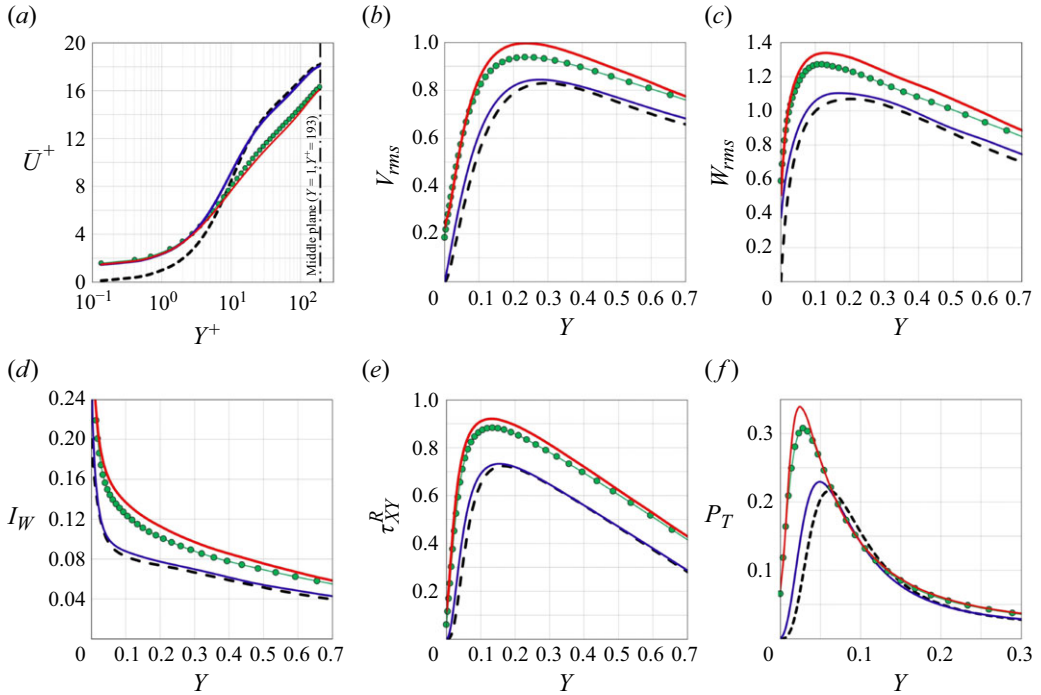


Figure 7. Distribution of the mean velocity (a) and behaviours of quantities of interest related to turbulence statistics (b–f) over the porous substrate TC_{20} : predictions of the homogenized simulation when the effective boundary conditions of the three velocity components are imposed (green lines with filled circles) or when transpiration is neglected (blue lines) are validated against results of the fine-grained simulation (red lines), while the dashed profiles are related to the smooth, impermeable channel case.

since it highlights the need of accounting for transpiration at the virtual boundary (Gómez-de-Segura *et al.* 2018a; Bottaro 2019; Lācis *et al.* 2020).

From inspection of figure 6, it is clear that the model captures well the trends of the mean velocity and the turbulence statistics displayed. The velocity profile can be analysed in terms of the slip velocity, $U_{slip}^+ = \bar{U}^+|_{Y=0}$; the shift in the intercept of the logarithmic velocity profile, ΔU^+ (taking the smooth channel case as a reference for the measurement and averaging the shift over the region $30 \lesssim Y^+ \lesssim 120$ (Ahmed *et al.* 2022b)); the percentage change in the bulk (channel-averaged) velocity through the free-fluid region, $\Delta U_{ch}^+ \%$ (taking the bulk velocity in a fully smooth channel, $U_{ch}^+ \approx 15.69$, as a reference); and the corresponding percentage change in skin-friction coefficient, $\Delta C_f \%$ (taking the smooth-channel value, $C_f = 2/(U_{ch}^+)^2 \approx 0.00813$, as a reference). The analysis performed here shows that, for the turbulent flow over the perturbed boundaries considered, the log-law is still valid (over $30 \lesssim Y^+ \lesssim 120$), yet it is shifted (relative to that for a smooth wall) by ΔU^+ such that the logarithmic profile reads

$$\bar{U}^+ = \frac{1}{\kappa} \ln(Y^+) + B + \Delta U^+, \tag{3.1}$$

where κ is the von Kármán constant and B is the intercept of the logarithmic profile for the flow over a corresponding smooth wall. Based on (3.1), if $\Delta U^+ < 0$ (respectively, $\Delta U^+ > 0$), the logarithmic profile is shifted downwards (upwards), and in general the skin-friction drag increases (decreases); this is consistent with the definition of the roughness function, ΔU^+ adopted by Gómez-de-Segura & García-Mayoral

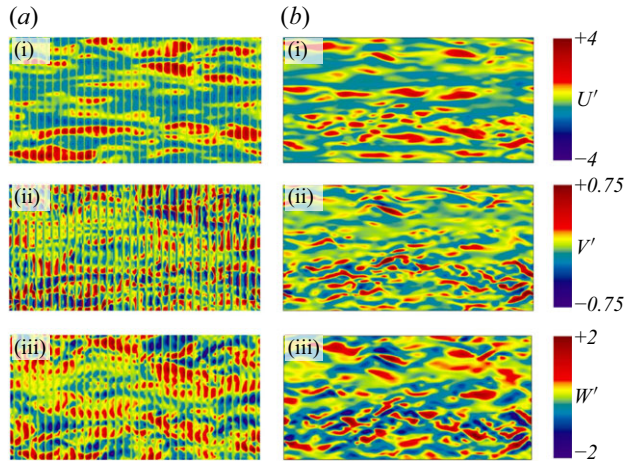


Figure 8. From (i) to (iii), instantaneous distributions of U' , V' and W' at the porous–free-fluid interface ($Y = 0$) for case TC_{20} . The fully resolved results (a) are compared with the homogenized ones (b).

(2019), Ibrahim *et al.* (2021) and Khorasani *et al.* (2022, 2024), which differs in sign from that originally introduced by Hama (1954) and Clauser (1954). According to (3.1), $\Delta U^+ < 0$ is generally accompanied by $\Delta U_{ch}^+ \% < 0$ and $\Delta C_f \% > 0$. The full feature-resolving simulation for the case chosen for validation (TC_{20}) yields $(U_{slip}^+, \Delta U^+, \Delta U_{ch}^+ \%, \Delta C_f \%) \approx (1.37, -2.76, -12.2 \%, +29.6 \%)$, while the values obtained from the model are, respectively, $(1.44, -2.33, -10.3 \%, +24.4 \%)$; a decrease in flow rate and, therefore, an increase in skin-friction coefficient is realized in both simulations. Moreover, the model predictions for the r.m.s. fluctuations of the velocity components at the fictitious interface ($Y = 0$) match well the results of the full simulation and deviate significantly from zero. In general, the accuracy of the macroscopic model is reasonable taking into account that the value of $\epsilon = 0.2$ ($\ell^+ \approx 40$) related to the porous substrate chosen for validation (TC_{20}) is rather large, meaning that microscopic and macroscopic length scales do not differ widely. On the other hand, it is obvious from figure 7 that the comparison with the fine-grained simulation is not satisfactory when the transpiration-free model is applied, where the mechanism of drag increase is idle, ΔU^+ is close to 0, and the trend of the turbulence statistics next to the fictitious boundary is similar to that of a smooth, impermeable channel (cf. Ibrahim *et al.* (2021)). A third, important, scenario is presented later in § 4, where the transpiration velocity boundary condition is imposed while \mathcal{K}_{yy} is set to zero, for the porous substrate to be modelled as a rough, impermeable wall. The discussion there centres around the evaluation of \mathcal{K}_{yy} for a porous bed which is bounded from the bottom, and on how the accuracy of the model is affected by neglecting the medium permeability of a deep, yet finite, substrate such as the one considered here for validation (figure 5).

Finally, figure 8 displays a comparison between the results of the full texture-resolving simulation and the homogenized one, concerning the fluctuating patterns of the three velocity components at the porous–free-fluid interface. This figure is added following one referee’s advice, with the purpose of providing the readers with the information needed to assess on their own how well the upscaled boundary conditions mimic the effect of the porous substrate on the turbulence.

3.2. Case studies: results and discussion

Numerical simulations were run for the channel flow over the different porous substrates (*TC*, *LC*, *TM*, *LM*), with four values of ϵ tested for each ($\epsilon = 0.05, 0.1, 0.15, 0.2$). The macroscopic model already validated was employed to study the 16 problems under consideration, with the Oseen-based upscaled coefficients contributing to the effective boundary conditions available in [table 1](#). The main results are presented and discussed below.

3.2.1. Mean velocity and skin-friction drag

In [table 2](#), the pitch distance and the macroscopic coefficients for each porous pattern are expressed in wall units based on the velocity scale $u_{\tau(\mathcal{M})}$; they are defined by

$$\ell^+ = \frac{\rho u_{\tau(\mathcal{M})} \ell}{\mu} = \epsilon Re_{\tau(\mathcal{M})}, \quad (3.2a)$$

$$\lambda_x^+ = \frac{\rho u_{\tau(\mathcal{M})} \hat{\lambda}_x}{\mu} = \epsilon Re_{\tau(\mathcal{M})} \lambda_x, \quad \lambda_z^+ = \epsilon Re_{\tau(\mathcal{M})} \lambda_z, \quad (3.2b)$$

$$\mathcal{K}_{xy}^{itf,+} = \epsilon^2 Re_{\tau(\mathcal{M})}^2 \mathcal{K}_{xy}^{itf}, \quad \mathcal{K}_{zy}^{itf,+} = \epsilon^2 Re_{\tau(\mathcal{M})}^2 \mathcal{K}_{zy}^{itf}, \quad \mathcal{K}_{yy}^+ = \epsilon^2 Re_{\tau(\mathcal{M})}^2 \mathcal{K}_{yy}. \quad (3.2c)$$

Values of the major quantities related to the behaviour of mean velocity through the free-fluid region are also listed in the table (refer to the definitions in § 3.1). The most significant finding is that reduction of the skin-friction drag coefficient (negative values of ΔC_f %, associated with positive ΔU^+ and ΔU_{ch}^+ %) is attainable only by the porous substrates formed by longitudinal inclusions (*LC* and *LM*), those characterized by streamwise-preferential slip lengths and interface permeabilities ($\lambda_x^+ > \lambda_z^+$, $\mathcal{K}_{xy}^{itf,+} > \mathcal{K}_{zy}^{itf,+}$). Such a favourable influence (up to 5 % reduction in C_f) takes place exclusively at relatively small values of ℓ^+ , a behaviour similar to that found by Gómez-de-Segura & García-Mayoral (2019) for this kind of permeable boundaries and analogous to that exhibited by riblets (Bechert & Bartenwerfer 1989; Garcia-Mayoral & Jiménez 2011a; Endrikat *et al.* 2021a,b; Wong *et al.* 2024). On the other hand, permeable beds consisting of transverse grains yield only drag increase, and this becomes more pronounced with ℓ^+ . For comparison purposes, the results obtained by normalizing results with the shear velocity of the bottom surface, $u_{\tau(\mathcal{B})}$, are given in [appendix B](#).

The behaviour of the sample quantities reported on the right-hand side of [table 2](#) for the four substrate configurations are graphically presented as function of the streamwise Navier-slip lengths in [figure 9](#). It is important to highlight the following features with reference to the trends of the figure.

- (i) As discussed in § 2.4, the first-order term in the effective boundary condition of the streamwise velocity yields a slip velocity at the permeable interface $U_{slip}^+ \approx \lambda_x^+ (\partial \bar{U}^+ / \partial Y^+) |_{Y=0} \approx \lambda_x^+$. [Figure 9\(a\)](#) shows that this linear dependence fits well with the results of the simulations, for the roughness amplitudes considered. Besides the omission of the higher-order term, the small percentage errors (up to ≈ 11 % in absolute value) may be attributed to the deviation of $(\partial \bar{U}^+ / \partial Y^+) |_{Y=0}$ from 1 because the parameters are expressed in wall units based on $u_{\tau(\mathcal{M})}$, and not the permeable-interface shear velocity $u_{\tau(\mathcal{B})}$. However, one can write $(\partial \bar{U}^+ / \partial Y^+) |_{Y=0} = (\partial \bar{U}^{+(\mathcal{B})} / \partial Y^{+(\mathcal{B})}) |_{Y=0} [(u_{\tau(\mathcal{B})} / u_{\tau(\mathcal{M})})]^2$, where $(\partial \bar{U}^{+(\mathcal{B})} / \partial Y^{+(\mathcal{B})}) |_{Y=0} \approx 1$ (provided that the Reynolds stress at $Y = 0$ is much

Substrate	Model coefficients						Sample results			
	ℓ^+	λ_x^+	λ_z^+	$\mathcal{K}_{xy}^{if,+}$	$\mathcal{K}_{zy}^{if,+}$	\mathcal{K}_{yy}^+	U_{slip}^+	ΔU^+	$\Delta U_{ch}^+ \%$	$\Delta C_f \%$
Smooth	0	0	0	0	0	0	0	0	0	0
TC_5	9.7	0.43	0.64	0.20	0.49	0.17	0.43	-0.33	-1.1 %	+2.1 %
TC_{10}	19.3	0.79	1.14	0.67	1.57	0.68	0.83	-0.77	-3.2 %	+6.7 %
TC_{15}	29.0	1.07	1.46	1.20	2.57	1.53	1.14	-1.55	-6.4 %	+14.2 %
TC_{20}	38.6	1.30	1.72	1.74	3.49	2.72	1.44	-2.33	-10.3 %	+24.4 %
LC_5	9.7	0.66	0.44	0.52	0.21	0.17	0.66	+0.15	+1.1 %	-2.1 %
LC_{10}	19.3	1.33	0.87	2.07	0.84	0.68	1.33	+0.08	+0.9 %	-1.9 %
LC_{15}	29.0	1.99	1.31	4.66	1.88	1.53	2.05	-0.54	-1.4 %	+2.8 %
LC_{20}	38.6	2.66	1.74	8.29	3.34	2.72	2.87	-1.63	-6.7 %	+15.0 %
TM_5	9.7	0.54	1.03	0.35	1.03	0.01	0.56	-0.61	-2.3 %	+4.7 %
TM_{10}	19.3	0.94	1.71	1.03	3.06	0.05	1.02	-1.38	-5.5 %	+12.0 %
TM_{15}	29.0	1.22	2.09	1.62	4.84	0.10	1.36	-2.09	-9.0 %	+20.9 %
TM_{20}	38.6	1.44	2.31	2.10	6.29	0.18	1.61	-2.56	-11.3 %	+27.0 %
LM_5	9.7	1.09	0.57	1.13	0.38	0.01	1.07	+0.33	+1.9 %	-3.7 %
LM_{10}	19.3	2.18	1.14	4.52	1.53	0.05	2.15	+0.45	+2.6 %	-5.0 %
LM_{15}	29.0	3.27	1.71	10.17	3.44	0.10	3.36	-0.33	-0.4 %	+0.7 %
LM_{20}	38.6	4.36	2.28	18.08	6.12	0.18	4.48	-0.94	-2.9 %	+6.1 %

Table 2. Values of the macroscopic coefficients characterizing the different configurations considered for the porous substrate, estimated in wall units with $Re_{\tau(\mathcal{M})} = 193$ and ϵ varied from 0.05 (subscript 5) to 0.2 (subscript 20). Major results are presented, with the normalization based on $u_{\tau(\mathcal{M})}$. Monitoring the progress of the mean bulk velocity U_{ch}^+ during 10 additional units of time, $\Delta U_{ch}^+ \%$ is found to differ by $\pm 0.2 \%$ at the most (and $\pm 0.07 \%$ on average) from the final values reported in the table.

smaller than the viscous stress), which results in the modified relation $U_{slip}^+ \approx [(u_{\tau(B)}/u_{\tau(\mathcal{M})})]^2 \lambda_x^+$. This expression enhances the predictions of the slip velocity (maximum error below 4 %), yet it cannot be employed *a priori*, since the values of the shear-velocity ratio are available only after numerical simulations have been conducted (cf. [appendix B](#)).

- (ii) It has been found convenient to express the roughness function as the difference between the shifts of the virtual origins of mean and turbulent flows, i.e. $\Delta U^+ \approx \ell_U^+ - \ell_{Turb}^+$ (Ibrahim *et al.* 2021). For small protrusion heights, Luchini *et al.* (1991) have shown that ΔU^+ takes the form $\Delta U^+ = \lambda_x^+ - \lambda_z^+ = \Delta \lambda^+$; in the present settings, this assumption holds only up to $|\Delta \lambda^+| \lesssim 0.25$; cf. [figure 9\(b\)](#). Also Gómez-de-Segura *et al.* (2018b) plotted the roughness function against the difference between the displacements of the virtual origins, and they did it for a variety of complex surfaces (anisotropic porous substrates, superhydrophobic surfaces, riblets and canopies), highlighting a behaviour ([figure 5](#) in their paper) qualitatively similar to that displayed in [figure 9\(b\)](#).
- (iii) As far as the trends of $\Delta C_f \% = (C_f - C_{f,smooth})/C_{f,smooth} \times 100 \%$ are concerned, the classical linearized relation $\Delta C_f \% = ((-\Delta U^+ / (2C_{f,smooth})^{-0.5} + (2\kappa)^{-1}) \times 100 \%$ is expected to align well with the results for small changes in C_f (Luchini 1996; Bechert *et al.* 1997). With $\Delta U^+ = \Delta \lambda^+$, $C_{f,smooth} = 0.00813$ and the von Kármán constant $\kappa = 0.4$, the linear dependence $\Delta C_f \% \approx -0.1 \Delta \lambda^+ \times 100 \%$ is valid provided that $|\Delta \lambda^+|$ remains sufficiently small, as confirmed in [figure 9\(d\)](#). Under the same condition, it can be shown that $\Delta U_{ch}^+ \% \approx -0.5 \Delta C_f \% \approx +0.05 \Delta \lambda^+ \times 100 \%$, which fits well the results in [figure 9\(c\)](#).

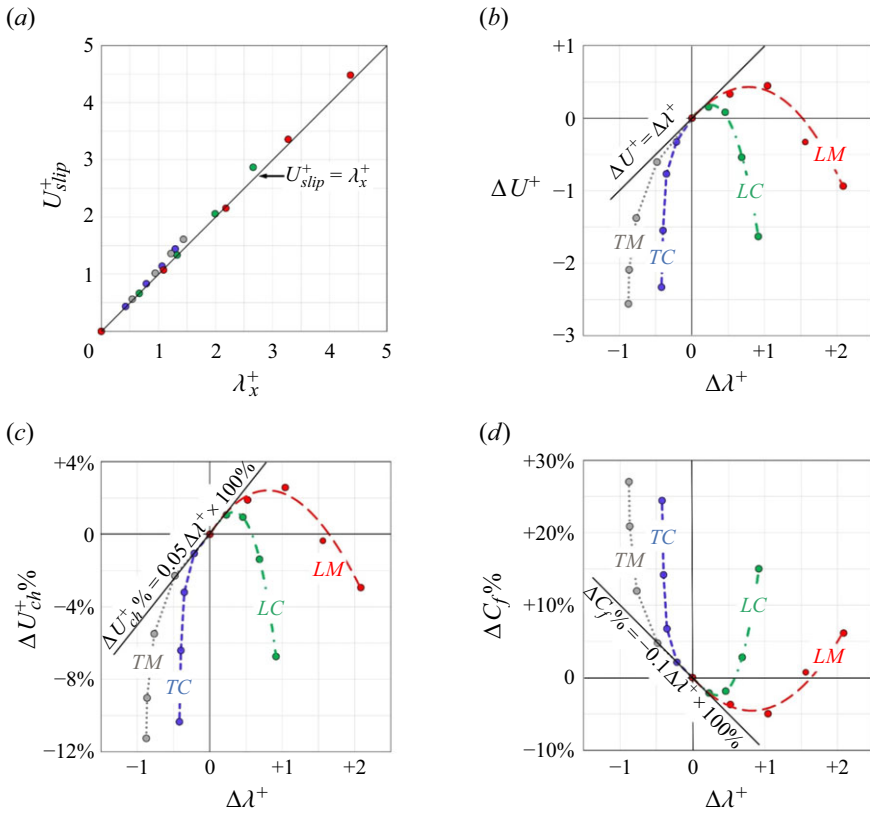


Figure 9. Dependence of (a) the slip velocity U_{slip}^+ on λ_x^+ and of (b) the shift of the logarithmic profile intercept ΔU^+ , (c) the percentage change in the bulk mean velocity $\Delta U_{ch}^+ \%$ and (d) the percentage change in the skin-friction coefficient $\Delta C_f \%$ on $\Delta\lambda^+ = \lambda_x^+ - \lambda_z^+$, for turbulent channel flows ($Re_{\tau(\mathcal{M})} = 193$) over the four types of permeable beds under study; cf. table 2. Simple linear relations fitting the behaviour of U_{slip}^+ with λ_x^+ and the performance of the other quantities at small values of $\Delta\lambda^+$ are presented.

(iv) It is notable that, at any fixed value of $\Delta\lambda^+$, the porous substrates *LM* and *TM* outperform the configurations *LC* and *TC* in terms of either maximizing the drag reduction or minimizing the drag increase. One possible justification is that the permeable beds constructed with modified cylinders (*LM* and *TM*) exhibit much smaller values of the medium permeability \mathcal{K}_{yy}^+ compared with those designed based on flat cylinders (*LC* and *TC*), as can be realized from table 2. This favourable feature enhances ΔU^+ by attenuating the transpiration velocity at the fictitious interface ($Y = 0$), an effect which can be perceived as a mitigation of the blowing and suction events. The influence of transpiration on ΔU^+ will be discussed in further detail in § 3.3.

In figure 10, the different results are plotted against the pitch distance, ℓ^+ . With regard to the slip velocity, assuming the simple linear relation $U_{slip}^+ \approx \lambda_x^+ = \ell^+ \lambda_x$ and recalling the trends of λ_x from table 1, one can expect that U_{slip}^+ changes linearly with ℓ^+ for the porous beds *LC* and *LM* since λ_x is independent of ℓ^+ for these streamwise-elongated patterns, in contrast to the spanwise-elongated patterns *TC* and *TM* for which the coefficient λ_x decreases with the increase of ℓ^+ on account of near-interface advection. These expectations agree with the behaviours displayed in figure 10(a). For small ℓ^+ values, the

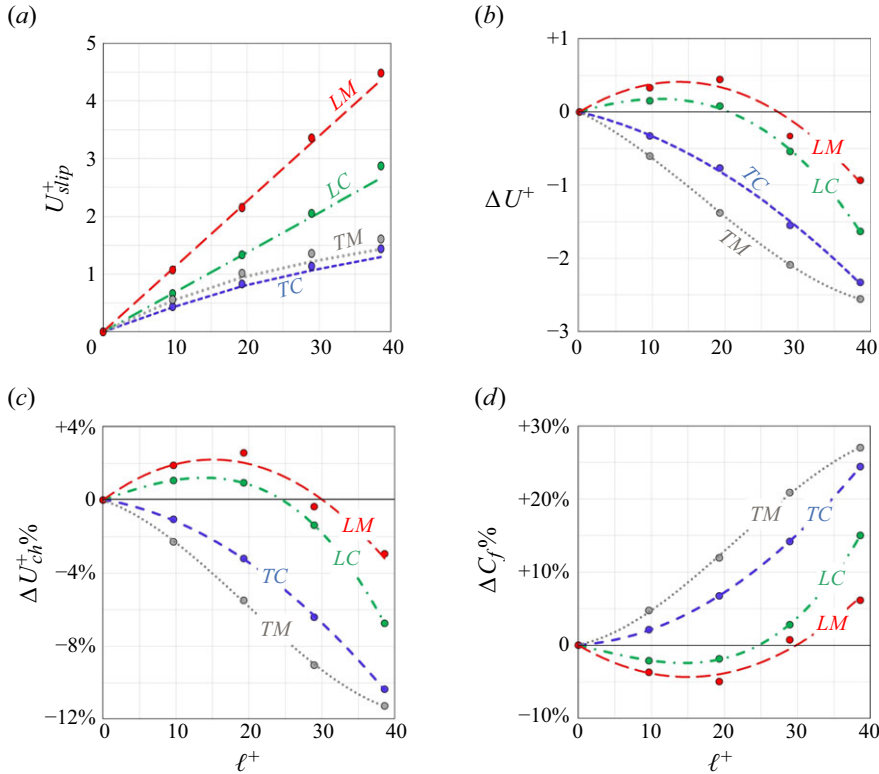


Figure 10. Dependence of major quantities characterizing the turbulent channel flow over the porous substrates under study on the pitch distance of the inclusions measured in wall units, $\ell^+ = \epsilon Re_{\tau(\mathcal{M})}$. Results of the homogenization-based DNS are plotted with filled circles. The lines in panel (a) represent the simple relation $U_{slip}^+ = \ell^+ \lambda_x$, while those in the other panels are simple fitting curves.

quantities ΔU^+ , $\Delta U_{ch}^+ \%$ and $\Delta C_f \%$ are directly proportional to $\Delta \lambda^+ = \ell^+ \Delta \lambda$ (Luchini 1996), where $\Delta \lambda$ is equal to $\lambda_x - \lambda_z$. Table 1 implies that $\Delta \lambda|_{LM} > \Delta \lambda|_{LC} > \Delta \lambda|_{TC} > \Delta \lambda|_{TM}$ with the first two positive and the last two negative. For a small value of ℓ^+ , one should therefore expect $\Delta U^+|_{LM} > \Delta U^+|_{LC} > \Delta U^+|_{TC} > \Delta U^+|_{TM}$ (and likewise for $\Delta U_{ch}^+ \%$ and $-\Delta C_f \%$) with the substrate LM yielding the maximum drag reduction and TM resulting in the maximum drag increase; cf. figure 10(b–d). Departing from the viscous regime, it is found that the drag reduction attainable by LM and LC peaks at some value of ℓ^+ between 10 and 20. The performance of these porous substrates then degrades, yet drag reduction is still achievable until a threshold within $20 \lesssim \ell^+ \lesssim 30$ is reached, beyond which drag increase takes place. Gómez-de-Segura *et al.* (2018a) studied highly connected porous media with streamwise-preferential permeability and attributed the aforementioned behaviour to the formation of drag-increasing spanwise-coherent rollers associated with a Kelvin–Helmholtz-like instability whose initiation is governed by the intrinsic permeability component \mathcal{K}_{yy}^+ of the medium. Finally, we should not forget that all results plotted in figures 9 and 10 are obtained via homogenization-based DNS. The accuracy of the trends displayed is thus dependent on the accuracy of the upscaling approach for each of the cases considered (in this respect, one may want to go back to the validation conducted considering the pattern TC_{20} in § 3.1).

3.2.2. The mechanism of drag increase/reduction

The influence of porous substrates on the near-interface turbulence is considered next. For sufficiently small values of ℓ^+ , the wall texture alters the structure of turbulence merely by shifting down its virtual origin by a distance $\ell_{Turb}^+ \approx \lambda_z^+$, whereas the effect is much more complicated beyond the viscous regime, especially with the increase in transpiration velocity. It is therefore useful to present and discuss some turbulence statistics of interest for the channel flow over selected porous beds of relatively large grain spacings/sizes (LM_{10} , longitudinal modified inclusions, $\ell^+ \approx 20$, the maximum drag reduction reported; LM_{20} , longitudinal modified inclusions, $\ell^+ \approx 40$, drag increase; TM_{10} , transverse modified inclusions, $\ell^+ \approx 20$, drag increase; TM_{20} , transverse modified inclusions, $\ell^+ \approx 40$, the maximum drag increase reported). The velocity profiles are plotted in figure 11(a). The turbulence-characterizing quantities plotted in figure 11(b) are chosen since, as shown by Ahmed *et al.* (2022b), their behaviours near the porous–free-fluid interface can be linked to the favourable/adverse effects of the permeable boundaries on friction drag. With focus on the peak values of V_{rms} , W_{rms} , τ_{XY}^R and P_T , and the distributions of I_W , it can be realized that the drag-reducing substrate (LM_{10}) yields results comparable to those in the reference case of turbulence over a smooth, impermeable wall; this applies also to the other drag-reducing patterns not considered in the figure, i.e. LM_5 , LC_5 , LC_{10} . Conversely, the drag-increasing ones result in intensified levels of these quantities. For instance, with TM_{20} , the peak values V_{rms} , τ_{XY}^R and P_T are larger than the values in a smooth channel by approximately 16%, 24% and 50%, respectively. The values of the quantities at the fictitious interface, $Y = 0$, are of particular interest in the present work and their correlations with ΔU^+ are explored in § 3.3; it is evident from the figure that significant values of V_{rms} are obtained at the plane $Y = 0$, in particular when ℓ^+ is sufficiently large, an important effect (Jiménez *et al.* 2001; Orlandi *et al.* 2003, 2006; Orlandi & Leonardi 2006, 2008) which would obviously be absent if transpiration were unaccounted for in the formulation of the model.

The quadrant analysis in figure 12 reveals details of the generation of the Reynolds stress, τ_{XY}^R , from the turbulent events taking place in the flow near the substrates LM_{10} and TM_{20} . In figure 12, the instantaneous distributions of (U', V') are displayed over the plane at $Y^+ \approx 1$, directly adjacent to the substrate–channel interface, and the plane at $Y^+ \approx 80$, well above the substrate. The phenomena can be classified into negative-production events (first and third quadrants, with $-U'V' < 0$) and positive-production ones (second and fourth quadrants, with $-U'V' > 0$); refer to, for instance, Wallace *et al.* (1972). Eventually, the Reynolds stress generated from the sum of the positive contributions from the ejection (second quadrant, bursting of low-speed fluid) and the sweep (fourth quadrant, inrush of high-speed fluid) events at any Y^+ level is generally larger than that arising from the sum of the contributions of the other two quadrants. The production of turbulence is dominated by the sweep event in the close vicinity of the boundary (cf. figure 12a,b), while ejection is dominant away from the wall (cf. figure 12c,d). For a better understanding, the contributions from the four quadrants to the Reynolds shear stress at a given time instant, evaluated over different $X - Z$ planes up to $Y^+ \approx 80$, are plotted in figure 12(e,f); they are obtained by integrating the values of $-U'V'$ related to each of the quadrants, separately, over the area occupied by the specific event and using the overall area of the $X - Z$ plane ($= 2\pi \times \pi$) as a weight. It is notable that ejection becomes dominant beyond a threshold within $Y^+ = 12-15$. All the findings above agree qualitatively with the results by Kim *et al.* (1987) in a channel delimited by smooth, impermeable walls. From a quantitative perspective, the production of turbulence via both ejection and sweep is clearly intensified for case TM_{20} (the porous substrate of maximum drag increase) compared with the

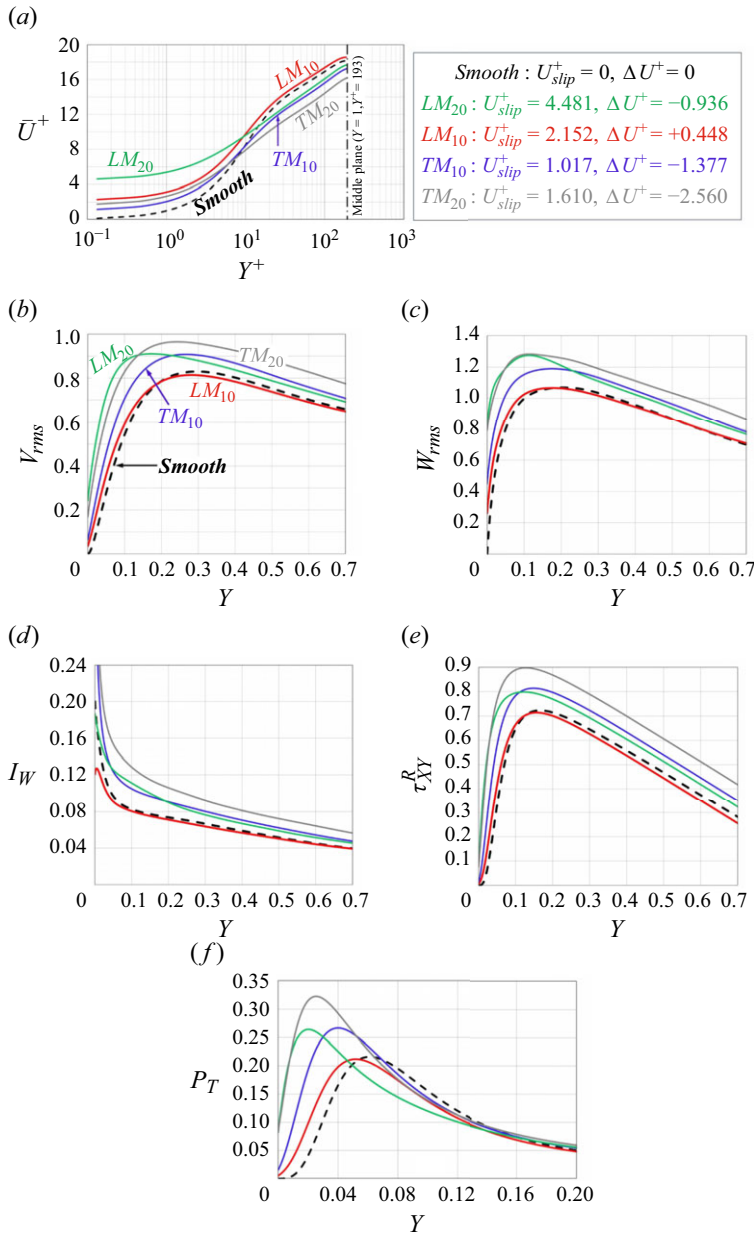


Figure 11. Predictions of the homogenization-based model for (a) the mean velocity profiles and (b–f) sample statistics for the channel flow ($Re_{\tau(\mathcal{M})} = 193$) over four different porous substrates.

levels with LM₁₀ (the substrate of largest drag reduction), at all the values of Y^+ considered.

In addition to the material presented in this section, it is beneficial to provide, via visualizations, some qualitative insights into the effects of the surface texture on the coherent structures (e.g. the pattern of streaks) and the turbulent events occurring in the inner region of the boundary layer; this is available in the Supplemental movie published online alongside this article. It might also be of interest, for future research focussed

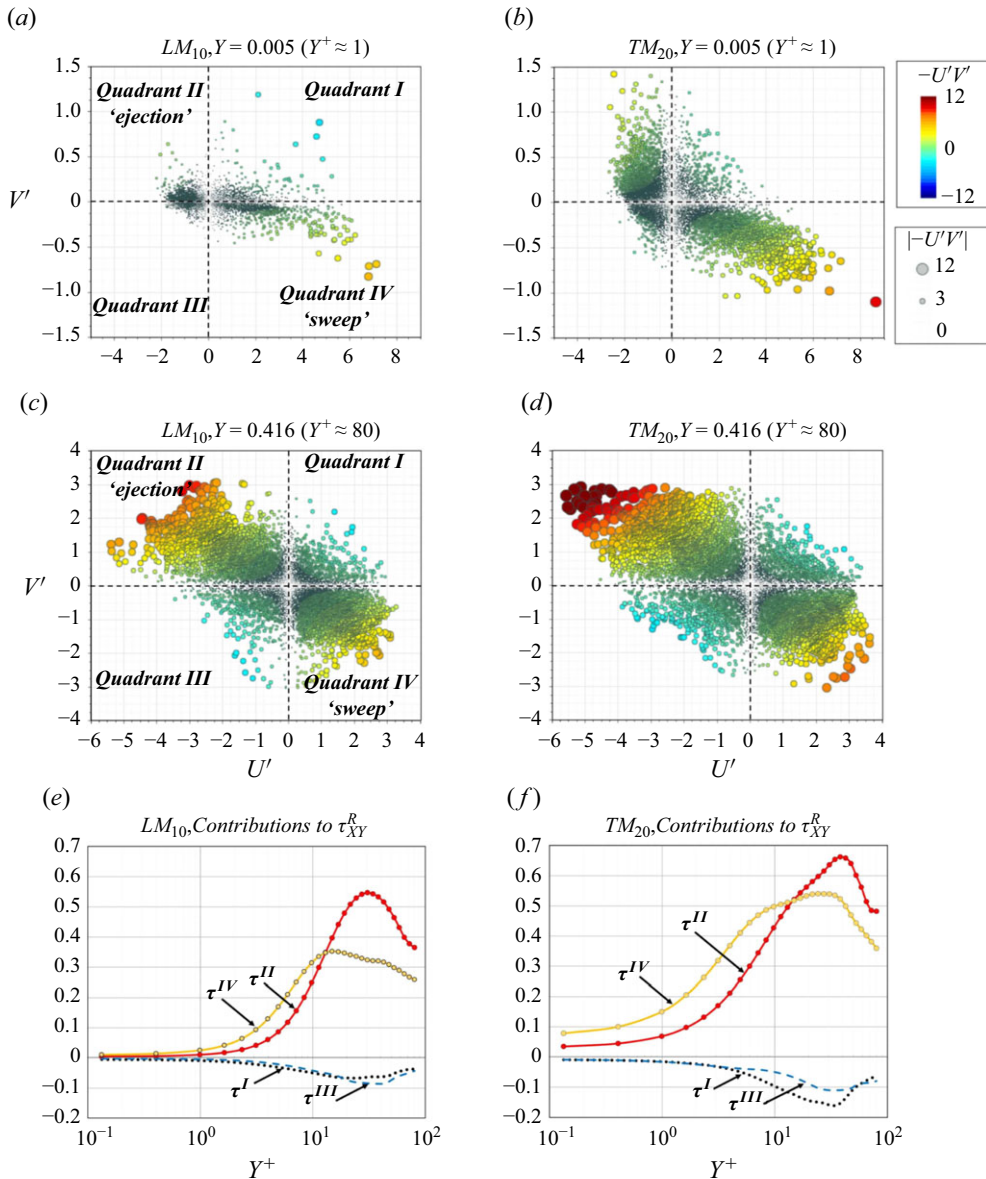


Figure 12. Quadrant analysis of the Reynolds shear stress, τ_{xy}^R , for turbulent channel flows ($Re_{\tau(\mathcal{M})} = 193$) over two different porous substrates (LM_{10} and TM_{20}). Instantaneous values of (U', V') throughout the planes at $Y = 0.005$ and $Y = 0.416$ (evaluated at all grid points) are shown in panels (a) to (d), while contributions to τ_{xy}^R from each quadrant are plotted in the bottom frames against $Y^+ = Y Re_{\tau(\mathcal{M})}$ up to the centreline of the channel.

on the flow physics, to explore how different substrate topologies affect the spectral density of the Reynolds stress and the premultiplied spectra of the velocity components next to the interface. This would probably need also a more extensive comparison between texture-resolving and modelled simulations, considering a large variety of porous microstructures. For these reasons, in the present contribution we prefer to address

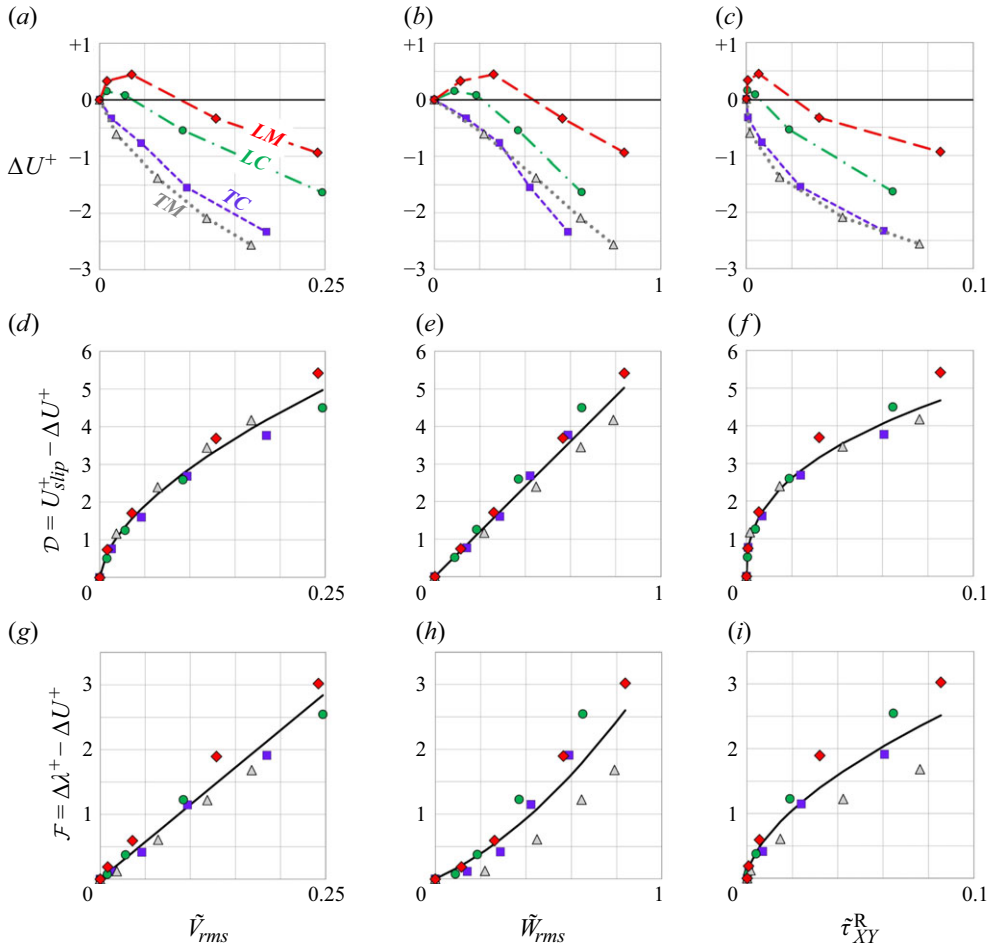


Figure 13. Dependence of ΔU^+ (a–c) and the related quantities \mathcal{D} (d–f) and \mathcal{F} (g–i) on turbulence-characterizing parameters of interest measured at the fictitious interface (at $Y = 0$). The filled symbols indicate results of the homogenized simulations for turbulent flow over the four substrate configurations under study (cf. figure 2), with ℓ^+ varied for each pattern as described in table 2, while the fitting relations (3.3–3.8) are plotted with solid lines in (d–i).

attention to the relation between the roughness function and the upscaled coefficients of the model.

3.3. In pursuit of a correlation for ΔU^+ over porous/textured walls

We proceed from the earlier discussion on figure 11, concerning how the near-wall distributions of some turbulence-characterizing parameters can control the mechanism of drag reduction/increase over the permeable boundaries, to explore the correlation between the roughness function ΔU^+ and the fictitious-interface values of quantities of particular interest: $\tilde{V}_{rms} = V_{rms}|_{Y=0}$, $\tilde{W}_{rms} = W_{rms}|_{Y=0}$ and $\tilde{\tau}_{XY}^R = \tau_{XY}^R|_{Y=0}$. Figure 13(a–c) reveals that the dependence of ΔU^+ on \tilde{V}_{rms} cannot be described by a universal function valid for all permeable boundaries; the same can be said for \tilde{W}_{rms} and $\tilde{\tau}_{XY}^R$. Conversely, each configuration yields a unique relationship, and even the general trends differ when porous substrates of streamwise-preferential permeability (LC and

LM, non-monotonic behaviour) are compared with those consisting of spanwise-elongated grains (TC and TM, strictly monotonic decrease). To explain this, let us assume conditions corresponding to a small value of \tilde{V}_{rms} fixed for the four patterns (e.g. $\tilde{V}_{rms} = 0.01$) and analyse the resulting ΔU^+ . While a fixed value of \tilde{V}_{rms} may imply that, for all the boundaries, the virtual origin of turbulence has the same shift from the $Y = 0$ plane (i.e. constant ℓ_{Turb}^+), the position of the virtual origin of the mean flow, $\ell_U^+ \approx \lambda_x^+$, can significantly differ according to the value of the streamwise Navier-slip length, λ_x^+ , for each wall, and, consequently, different values of the roughness function $\Delta U^+ = \ell_U^+ - \ell_{Turb}^+$ are obtained. In the search of a function displaying a universal behaviour, we follow two separate paths.

The first path relies on analysing the mean velocity profile, $\bar{U}^+(Y^+)$, over each of the permeable substrates to monitor the upward shifts of the velocity at matched Y^+ values, taking the profile over a smooth, impermeable wall as a reference (for instance, cf. figure 11a). Such a velocity shift is, by definition, equal to U_{slip}^+ at $Y = 0$ and to ΔU^+ in the logarithmic region. Whether ΔU^+ is positive or negative, it is $U_{slip}^+ > \Delta U^+$ for all textured boundaries (for $\ell^+ = 0$, the smooth, impermeable wall is retrieved, and the limit $U_{slip}^+ = \Delta U^+ = 0$ is reached). The function $\mathcal{D} = U_{slip}^+ - \Delta U^+ \geq 0$ can therefore be defined to indicate the depression in the velocity shift when moving from the wall to the logarithmic region; it is plotted against the turbulence parameters in figure 13(d-f).

In the second path, we proceed from the fact that the approximation $\Delta U^+ = \Delta \lambda^+$ holds only for small surface roughness, while a further reduction in the value of the roughness function occurs with the increase of ℓ^+ , i.e. $\Delta U^+ = \Delta \lambda^+ - \mathcal{F}$, with the newly defined function $\mathcal{F} \geq 0$. The behaviour of \mathcal{F} is shown in figure 13(g-i).

Both functions \mathcal{D} and \mathcal{F} increase monotonically with each of \tilde{V}_{rms} , \tilde{W}_{rms} and $\tilde{\tau}_{XY}^R$, and it can be realized from figure 13(d-i) that, even from a quantitative point of view, general trends emerge. Eventually, the following fitting relationships can be proposed (together with their accuracy levels):

$$\mathcal{D} = 11.5 \times [\tilde{V}_{rms}]^{0.6}, \quad NRMS_{error} \approx 11 \%, \quad (3.3)$$

$$\mathcal{D} = 6 \times \tilde{W}_{rms}, \quad NRMS_{error} \approx 13 \%, \quad (3.4)$$

$$\mathcal{D} = 12.5 \times [\tilde{\tau}_{XY}^R]^{0.4}, \quad NRMS_{error} \approx 11 \%, \quad (3.5)$$

$$\mathcal{F} = 11.5 \times \tilde{V}_{rms}, \quad NRMS_{error} \approx 18 \%, \quad (3.6)$$

$$\mathcal{F} = 1.8 \times [\tilde{W}_{rms}]^2 + 1.6 \times \tilde{W}_{rms}, \quad NRMS_{error} \approx 37 \%, \quad (3.7)$$

$$\mathcal{F} = 11 \times [\tilde{\tau}_{XY}^R]^{0.6}, \quad NRMS_{error} \approx 29 \%, \quad (3.8)$$

where the normalized r.m.s., $NRMS_{error}$, is evaluated by dividing the conventional RMS_{error} by the mean value of either \mathcal{D} or \mathcal{F} . The ranges of validity of the relations proposed are

$$0 \leq \tilde{V}_{rms} \lesssim 0.25, \quad 0 \leq \tilde{W}_{rms} \lesssim 0.85, \quad 0 \leq \tilde{\tau}_{XY}^R \lesssim 0.085. \quad (3.9)$$

In the remainder of this section, we aim to demonstrate (i) that transpiration strongly controls the depression in the velocity shift over a wide range of textured boundaries and

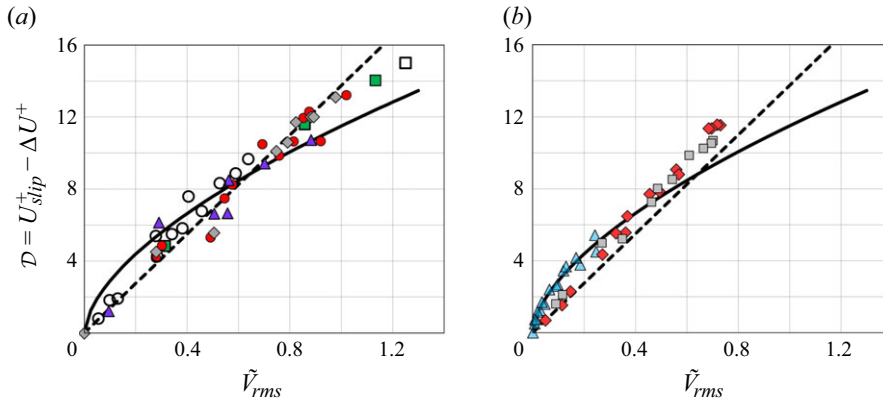


Figure 14. Values of the parameter \mathcal{D} plotted against the r.m.s. of the turbulent fluctuations in the wall-normal velocity at the plane $Y = 0$. In panel (a), results from the literature for channels roughened with streamwise-elongated, spanwise-elongated or three-dimensional elements are shown: blank square, Cheng & Castro (2002); red circles, Leonardi *et al.* (2003); purple triangles, Orlandi & Leonardi (2006); green squares, Burattini *et al.* (2008); grey diamonds, Orlandi & Leonardi (2008); blank circles, Hao & García-Mayoral (2025). In panel (b), the results of Hao & García-Mayoral (2025) for symmetric channels bounded by either deep (red diamonds) or shallow (grey squares) porous substrates are plotted, together with the values of the present homogenization-based simulations (light-blue triangles). Solid lines refer to correlation (3.3), while the linear relationship by Orlandi & Leonardi (2008) is plotted with dashed lines.

(ii) that correlating \tilde{V}_{rms} to the macroscopic coefficients of the homogenization model permits the use of (3.3) and (3.6) for an *a priori* estimate of the roughness-function-related parameters \mathcal{D} and \mathcal{F} .

Orlandi *et al.* (2003) demonstrated that the principal characteristics of the flow over a rough surface are closely related to the presence of wall-normal velocity distribution at the interface between the protrusions and the overlying turbulent boundary layer. A more formal description of this dependence has been proposed by Orlandi *et al.* (2006) and Orlandi & Leonardi (2006) who found good correlation between the quantity $\mathcal{D} = U_{slip}^+ - \Delta U^+$ and the r.m.s. fluctuations of the wall-normal velocity at the plane passing through the crests of the roughness elements. Later, Orlandi & Leonardi (2008) explored the relationship between \mathcal{D} and \tilde{V}_{rms} for walls with different textures, by collecting and plotting many results from the literature (Cheng & Castro 2002; Leonardi *et al.* 2003; Orlandi & Leonardi 2006; Burattini *et al.* 2008; Flores & Jiménez 2006) together with new ones related to the flow over surfaces roughened with longitudinal/transverse bars or various three-dimensional patterns. They concluded their study proposing the correlation $\mathcal{D} = (B/\kappa) \tilde{V}_{rms}$, with B and κ as by (3.1). Most of the data considered by Orlandi & Leonardi (2008) in addition to the recent results by Hao & García-Mayoral (2025) are presented in figure 14(a); the strong correlation between \mathcal{D} and \tilde{V}_{rms} is evident, and the linear relationship by Orlandi & Leonardi (2008), plotted with $B = 5.5$ and $\kappa = 0.4$ is found to perform well, where $NRMSE_{error}$ is below 12%. Interestingly, good correlation between \mathcal{D} and \tilde{V}_{rms} can also be realized in figure 14(b) for the turbulent flow over permeable boundaries, based on the values reported by Hao & García-Mayoral (2025) plotted next to the results of the present macroscopic DNS; the $NRMSE_{error}$ for Orlandi–Leonardi relationship is approximately 23%. With regard to the present correlation (3.3), the deviations are comparable to those reported above, with $NRMSE_{error} \approx 14\%$ for the rough walls and $\approx 18\%$ for the porous boundaries, even for values of \tilde{V}_{rms} much larger than the validity limit (3.9) of our simulations. Figure 14 thus confirms that \tilde{V}_{rms} is a key

parameter which controls the roughness function in the turbulent flow over rough/porous boundaries and that (3.3) performs well even for quite large values of \tilde{V}_{rms} . The major difficulty in putting (3.3), or Orlandi–Leonardi correlation, to practical use is that \tilde{V}_{rms} is not available until a full simulation of the turbulent flow above a textured wall is conducted.

The crux of the matter is thus the search of a simplified expression for \tilde{V}_{rms} , as function of the macroscopic coefficients which permit to describe the near wall flow. After some efforts, we have found that the parameter Ψ defined as

$$\Psi = \left(\frac{\mathcal{K}_{xy}^{itf,+}}{\lambda_x^+} + \frac{\mathcal{K}_{zy}^{itf,+}}{\lambda_z^+} + \sqrt{\mathcal{K}_{yy}^+} \right) \left(\frac{\lambda_z^+}{\lambda_x^+} \right)^{0.25} \tag{3.10}$$

is well correlated to \tilde{V}_{rms} , as shown in figure 15. It is worth highlighting that (3.10) is based on the coefficients present in the boundary condition for the transpiration velocity (2.21b): the parameters $(\mathcal{K}_{xy}^{itf,+}/\lambda_x^+)$ and $(\mathcal{K}_{zy}^{itf,+}/\lambda_z^+)$ appear when the streamwise/spanwise Navier-slip conditions $(\partial\hat{u}/\partial\hat{y}) + (\partial\hat{v}/\partial\hat{x})|_0 = (\hat{u}|_0/\hat{\lambda}_x)$ and $((\partial\hat{w}/\partial\hat{y}) + (\partial\hat{v}/\partial\hat{z}))|_0 = (\hat{w}|_0/\hat{\lambda}_z)$ are substituted into the second and the third terms on the right-hand side of (2.21b) and the equation is recast in wall units, while $\sqrt{\mathcal{K}_{yy}^+}$ quantifies the role of the intrinsic permeability for porous boundaries. The presence of $(\lambda_z^+/\lambda_x^+)$ in (3.10) permits us to differentiate walls with spanwise-preferential slip ($\lambda_z^+ > \lambda_x^+$) from those exhibiting preferential streamwise slip ($\lambda_x^+ > \lambda_z^+$), and implies that, for the same values of $(\mathcal{K}_{xy}^{itf,+}/\lambda_x^+)$, $(\mathcal{K}_{zy}^{itf,+}/\lambda_z^+)$ and $\sqrt{\mathcal{K}_{yy}^+}$, relatively stronger transpiration is associated with the former wall patterns (e.g. substrates with transverse inclusions). Based on the data plotted in figure 15, we can propose the fitting equation

$$\tilde{V}_{rms} = 0.00075 \Psi^3 + 0.002 \Psi^2, \tag{3.11}$$

for which the $NRMSE_{error}$ is less than 10%. Substituting (3.11) into (3.3) and (3.6), we finally obtain the following expressions for the roughness-function-related quantities:

$$\mathcal{D} = U_{slip}^+ - \Delta U^+ = 11.5 \times (0.00075 \Psi^3 + 0.002 \Psi^2)^{0.6}, \tag{3.12}$$

$$\mathcal{F} = \Delta\lambda^+ - \Delta U^+ = 11.5 \times (0.00075 \Psi^3 + 0.002 \Psi^2), \tag{3.13}$$

valid up to $\Psi \approx 6$. These expressions are plotted in figure 16 together with the results obtained from the homogenization-based DNS conducted for the porous patterns *TC*, *LC*, *TM* and *LM*. Estimates of \mathcal{D} and \mathcal{F} for the turbulent flow over a perturbed wall of given microstructure and given value of $\ell^+ = \epsilon Re_{\tau(\mathcal{M})}$ are thus available provided (i) ℓ^+ is lower than approximately 40, and (ii) outer layer similarity is maintained.

As a side remark, we observe that the relations obtained in this section have been generated by fitting data that pertain to the turbulent flow in a channel with asymmetric boundaries, and all the quantities (mean streamwise velocity, turbulence statistics and macroscopic coefficients) have been normalized with the macroscopic-pressure-gradient-based shear velocity, $u_{\tau(\mathcal{M})}$. Since different choices appear in the literature, we provide in appendix B key quantities scaled with the total stress at the bottom wall. It is also shown that (3.12) and (3.13) remain reasonably accurate, independently of the choice of u_{τ} .

3.4. Can we make a priori predictions?

It is useful to assess the accuracy of (3.12) and (3.13) for the turbulent flow over perturbed boundaries different from the porous ones based on which these correlations have been generated. In particular, we choose to check the generality of the relations

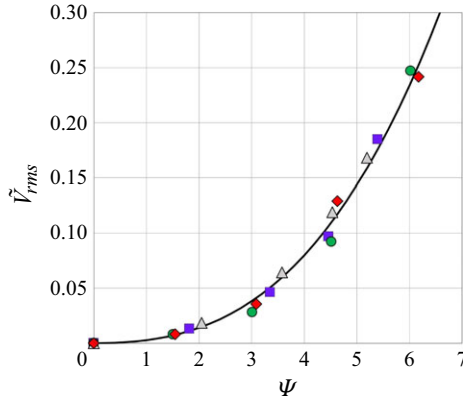


Figure 15. The r.m.s. of turbulent fluctuations in the transpiration velocity at $Y=0$, plotted against the compound macroscopic parameter Ψ for the different porous patterns considered (same symbols as in figure 13). The solid line represents a third-order polynomial fitting.

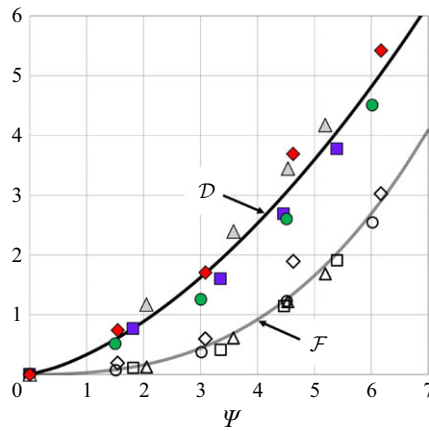


Figure 16. The roughness-function-related quantities \mathcal{D} and \mathcal{F} , plotted against the parameter Ψ for the different porous patterns considered (same symbols as in figure 13, filled for \mathcal{D} and empty for \mathcal{F}). Correlations (3.12) and (3.13) are plotted with solid lines.

above by validating them against existing numerical/experimental results for the motion over rough, impermeable walls ($\mathcal{K}_{yy} = 0$) with either two- or three-dimensional wall corrugations. The results in figure 17 are related to the turbulent flow ($Re_{\tau(\mathcal{M})} = 182.70$) in a symmetric channel delimited by walls roughened with in-line patterns of cubical protrusions having side length e and pitch $\ell = 2e$. The Oseen-based upscaled coefficients, sensitive to the level of near-interface advection and hence to the value of ℓ^+ , are evaluated for $\ell^+ = (0, 12, 23.9, 35.9, 47.8)$ and are plotted in figure 17(a). The corresponding values of Ψ are $(0, 2.84, 4.39, 5.78, 7.29)$, and are used to predict the behaviour of the quantity \mathcal{D} in figure 17(b). These predictions are compared with the numerical results of the feature-resolving simulations by Hao & García-Mayoral (2025), and good agreement is observed. To highlight the need of incorporating near-wall advection into the homogenization model, the calculations have been repeated by setting Re_{slip} equal to 0 in (2.24) and (2.25), and significant errors in the predictions of \mathcal{D} are found when

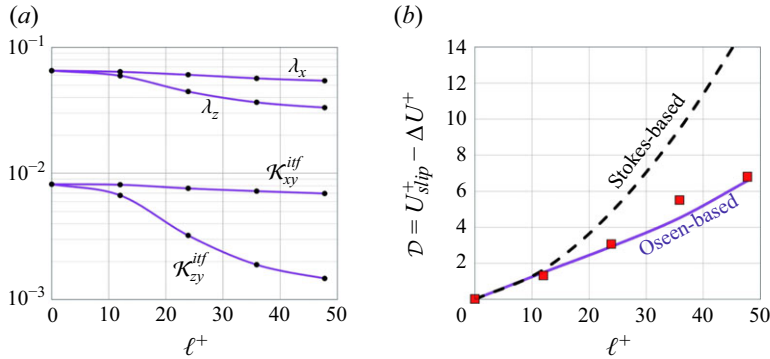


Figure 17. Turbulent flow ($Re_\tau \approx 180$) in a symmetric channel whose top/bottom boundaries are roughened with cubes (in-line arrangement) of size-to-pitch ratio $e/\ell = 0.5$, with the spacing in wall units, $\ell^+ = \epsilon Re_\tau(\mathcal{M})$, varied up to 50. Values of the macroscopic coefficients are plotted against ℓ^+ in panel (a). In panel (b), the behaviour of the parameter \mathcal{D} based on (3.12) is shown (blue curve), and is validated against the results by Hao & García-Mayoral (2025) obtained from full simulations (squares). The black dashed curve refers to the predictions of (3.12) when Ψ is evaluated with the Stokes-based upscaled coefficients, neglecting near-wall inertia; they are $\lambda_x = \lambda_z \approx 0.0653$ and $\mathcal{K}_{xy}^{if} \approx \mathcal{K}_{zy}^{if} = 0.0083$.

ℓ^+ exceeds 10. In fact, the Stokes-based results coincide with the Oseen-based ones for $\ell^+ \lesssim 10$, a threshold similar to that reported by Ahmed & Bottaro (2024) for laminar channel flows. Since $\Delta U^+ = U_{slip}^+ - \mathcal{D}$, the calculation of the roughness function based on the values obtained for \mathcal{D} requires knowledge of the slip velocity, U_{slip}^+ . It may be tempting to use the approximation $U_{slip}^+ = \lambda_x^+ (\partial \bar{U}^+ / \partial Y^+) |_{Y=0} \approx \lambda_x^+$, but care must be exerted, since significant errors appear in the predicted U_{slip}^+ as ℓ^+ becomes large, as a result of the large Reynolds stress generated at the channel virtual boundary in $Y = 0$ (Hao & García-Mayoral 2025). It is the approximation $(\partial \bar{U}^+ / \partial Y^+) |_{Y=0} = 1$ which eventually breaks down. In fact, based on the values of U_{slip}^+ and λ_x^+ reported by Hao & García-Mayoral (2025), we observe that the absolute deviations between the two quantities, for $\ell^+ = (12, 23.9, 35.9, 47.8)$, are, respectively, (1 %, 4 %, 28 %, 53 %). If we substitute $U_{slip}^+ = \lambda_x^+$ into (3.12), with the Oseen-based coefficients, we obtain $\Delta U^+ \approx (-0.73, -1.48, -2.49, -4.01)$, progressively deviating from the values computed by Hao & García-Mayoral (2025): $\Delta U^+ \approx (-0.50, -1.69, -3.77, -4.91)$.

The next case examined is that of riblets. Rather than explicitly using the expression recalled earlier, $\Delta U^+ = \ell_U^+ - \ell_{Turb}^+$, which is not predictive unless turbulent simulations are conducted for any shape of the riblets (or a model allowing for *a priori* predictions of ℓ_{Turb}^+ is formulated, e.g. the ‘viscous vortex model’ by Wong *et al.* (2024)), we employ (3.13). Clearly, when Ψ is vanishingly small the relationship (3.13) yields the classical viscous approximation $\Delta U^+ = \Delta \lambda^+$ (Luchini 1996; Garcia-Mayoral & Jiménez 2011a). Conversely, the behaviour of the roughness function can deviate significantly from this linear equation as ℓ^+ increases and transpiration becomes more pronounced. Different ribletted surfaces are shown in figure 18. For each geometry, the macroscopic coefficients are calculated (appendix C) and expressed in wall units by applying (3.2b) and (3.2c) for different spacings $\ell^+ = \epsilon Re_\tau(\mathcal{M})$ within the range considered ($0 \leq \ell^+ \leq 36$); the values of Ψ are accordingly between 0 and 7.4. The predictions in the form ΔU^+ versus ℓ^+ , plotted with blue solid lines, are validated against the DNS results by Wong *et al.* (2024) and the experimental findings by Bechert *et al.* (1997); a reasonably good agreement can be

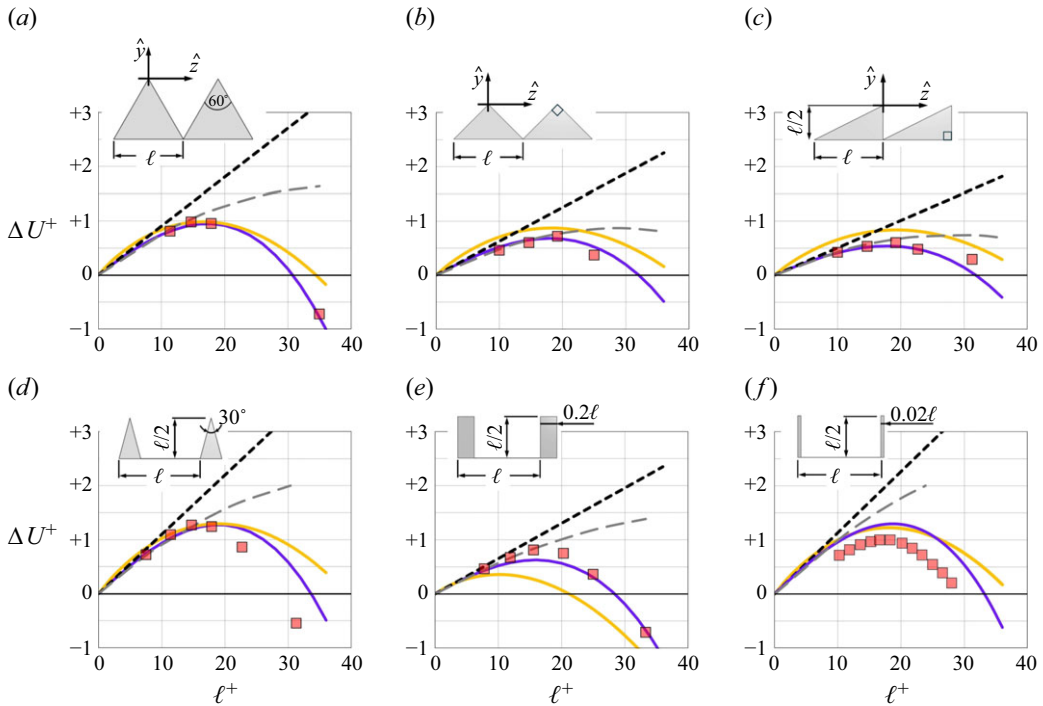


Figure 18. Behaviour of ΔU^+ with the increase in ℓ^+ , for the turbulent flow over surfaces with different shapes of riblets. The proposed correlations (\mathcal{D} -based (3.12), black solid lines; \mathcal{F} -based (3.13), blue solid lines) are validated against relevant DNS/experimental results from the literature (red symbols). The literature results plotted are by (a–e) Wong *et al.* (2024) and (f) Bechert *et al.* (1997); the latter were reported originally in terms of $(\Delta C_f/C_{f,smooth})$ and the corresponding values of ΔU^+ are obtained here employing the relation $\Delta U^+ = -(\Delta C_f/C_{f,smooth}) [(2C_{f,smooth})^{-0.5} + 1.25]$. In all panels, the thick black dashed lines represent the simple linear dependence $\Delta U^+ = \lambda_x^+ - \lambda_z^+ = (\lambda_x - \lambda_z) \ell^+$, while the grey dashed lines (wide dashes) show the predictions for ΔU^+ given by Wong *et al.* (2024) based on the so-called ‘viscous vortex model’.

ascertained from the figure, including the deviation from the linear dependence departing from the viscous regime, the performance degradation when the pitch distance exceeds a threshold between 15 and 20, and eventually the drag increase for large riblets’ periodicity. For larger values of ℓ^+ , not considered in the figure, predictions of the correlation are questionable since the resulting values of Ψ are significantly beyond the applicability range of the present correlation. For instance, Gatti *et al.* (2020) studied the turbulent flow over trapezoidal riblets (similar to those in figure 18d but with angle of 53.5° and height equal to 0.476ℓ) and found that ΔU^+ tends to become almost constant for ℓ^+ larger than approximately 60, a behaviour which cannot be captured by (3.13). Another point to be mentioned is that, for the ribletted surfaces examined in figure 18, the \mathcal{D} -based predictive relationship (3.12), with U_{slip}^+ set to λ_x^+ , yields results for ΔU^+ (plotted with orange solid lines) which are generally of lower accuracy than those obtained from (3.13). In addition, the viscous-vortex-model-based predictions of the roughness function, provided by Wong *et al.* (2024), are added to the figure; they generally exhibit reasonable accuracy up to the optimal ℓ^+ value for each ribletted surface (i.e. that corresponding to the maximum attainable drag reduction).

It is worth concluding this section with some notes of caution as to the applicability of our predictive correlations.

- (i) The expressions (3.12) and (3.13) are formulated based on the results of 16 homogenization-based DNS, considering only four configurations of the porous substrate; all cases relate to transversely isotropic patterns and are characterized by a unique value of porosity, $\theta = 0.5$. More work is certainly needed before the generality of these predictive relationships can be fully confirmed. This is also brought to attention in view of the possible deviations between the upscaling-based numerical results (employed to obtain all the trends/relationships in this paper) and the real values of the quantities of interest, attainable for example via high-fidelity feature-resolving DNS.
- (ii) There are configurations for which the two proposed correlations may not be tenable. An example is the case of a superhydrophobic wall, with a flat and undeformable liquid–gas interface. In this case $\tilde{V}_{rms} = 0$ and (3.12) reduces to $\Delta U^+ = U_{slip}^+$ (incidentally, also the expression $\mathcal{D} = (B/\kappa) \tilde{V}_{rms}$ of Orlandi & Leonardi (2008) yields the same result). Since $U_{slip}^+ \approx \lambda_x^+$ the roughness function would then have a value larger than that of the conventional viscous approximation, $\Delta U^+ = \lambda_x^+ - \lambda_z^+$ (which is retrieved by the \mathcal{F} -based relationship (3.13)). For the case of superhydrophobic ribs it has been shown by Luchini (2015) that results for ΔU^+ obtained with either no-slip/no-shear boundary conditions or with a homogenized condition collapse well with the linear, viscous approximation until $\ell^+ \approx 30$.
- (iii) The good agreement between the predictions of (3.13) and the reference results for ΔU^+ in figure 18 does not imply that the correlation captures, for example, the initiation of a Kelvin–Helmholtz instability past some threshold value of ℓ^+ . We believe that our correlations represent an improvement over linear, viscous results (dashed lines in figure 18) to predict the roughness function, but we would not want to push this as far as stating that they capture the physics at large values of ℓ^+ . From a mathematical perspective, (3.13) appears to reasonably quantify drag reduction up to and beyond its maximum attainable value, for each ribletted surface considered.

4. Assumptions and range of validity of the model

It is necessary to highlight and properly assess the validity of the assumptions and simplifications adopted in the present work, considering the physical problem and the upscaling approach. Here, we focus on the following issues.

- (i) The effect of near-wall advection appears in the homogenization model through an Oseen-like linearization of the momentum equation governing the microscale problem. This approximation, described in § 2.2, requires the choice of a streamwise convective speed representative of the flow near the porous–free-fluid interface (for instance, refer to the near-interface behaviour of \bar{U}^+ displayed in figure 5). The slip velocity \hat{u}_{slip} , averaged over the fictitious interface, is used in the present work as a characteristic uniform scale to linearize the problem, and with this simple assumption a good agreement between the model predictions and the results of the fine-grained DNS is obtained (§ 3.1). However, there are other options which are ‘reasonable’, albeit more complicated, that could be adopted, for example assigning a distribution of the streamwise velocity component, as function of the wall-normal coordinate, going from the Darcy’s velocity \hat{u}_{darcy} in the deep porous region to the slip velocity \hat{u}_{slip} at $\hat{y} = 0$ and, finally, to a linearly increasing behaviour for $\hat{y} > 0$; clearly, this choice requires an approximation of the way the velocity decays below

the porous–free–fluid interface. For future research, near-interface inertia may be taken into account with a fully nonlinear model, rather than with the current Oseen linearization. This can be achieved by the use of adjoint homogenization (Bottaro 2019). Furthermore, it would be interesting to explore how the values of the upscaled coefficients estimated from the different approaches compare with those predicted by machine–learning algorithms for a large variety of wall microstructures.

- (ii) The normalization adopted, embodied by equations (2.2a)–(2.2c), implies that the characteristic time scale of the fluid within the porous medium is much larger than the temporal scale of phenomena in the free–fluid domain. This is corroborated by results of several, previous texture-resolving simulations conducted under conditions similar to the present ones. Further, to ensure the absence of time-dependent effects in the present microscopic closure problems, we have numerically solved them with a time-dependent solver for values of Re_{slip} up to 60, eventually always reaching steady solutions. Should near-wall transient effects become significant, for example beyond some critical value of Re_{slip} function of the geometry of the porous substrate, time should be incorporated into the upscaling framework and the effective interface conditions would involve convolution kernels, similar to the case of poroelastic interfaces (Zampogna *et al.* 2019b). Then, because of phenomena such as unsteady vortex shedding near the porous–free–fluid boundary, sufficiently large microscopic elementary cells (possibly consisting of several geometric unit cells) must be used to solve the closure problems (Aagnaou *et al.* 2016).
- (iii) The first term in the transpiration velocity boundary condition (2.21b) is associated with the vertical gradient of the normal stress S_{22} and includes the intrinsic medium permeability \mathcal{K}_{yy} as a macroscopic coefficient. The parameter \mathcal{K}_{yy} vanishes by definition for rough, impermeable walls, while it can be easily evaluated for a deep porous bed from the solution of a Stokes system on a triply periodic unit cell, imposing unit forcing along y . From a theoretical perspective, this approach assumes that the porous region is formally infinite in depth, for periodicity to perfectly apply along y . In practical situations, permeable substrates are, conversely, of finite depth and typically bounded at the bottom in $\hat{y} = -h$ (as in the pattern considered in figure 5). Since a correct transpiration velocity condition is sensitive mainly to the flow characteristics in a layer around the interface at $\hat{y} = 0$, we believe that the procedure followed to evaluate \mathcal{K}_{yy} holds also for porous substrates bounded from below, at least as long as their depth is sufficiently large. If one were, on the other hand, to solve a Stokes system (with unit forcing imposed along y) on a unit cell periodic in x and z and extending all the way to the bottom impermeable boundary, then the result $\mathcal{K}_{yy} = 0$ would be found; as a consequence, the transpiration boundary condition (at least, up to second-order accuracy in ϵ) would be free of a velocity–pressure coupling term (a similar issue was treated by Sharma & García-Mayoral (2020) in the evaluation of the wall-normal flow impedance for a canopy with a bottom, impermeable boundary). In this regard, it is pertinent to refer to the study by Hao & García-Mayoral (2025) on porous beds formed by staggered cubes, where they concluded that substrates deeper than approximately 50 viscous units can be classified as ‘sufficiently deep’. Under this condition, the turbulent flow perceives the substrate as deep enough to exhibit its permeable character fully such that the flow characteristics become almost insensitive to any further increase in the depth. Since the grains’ pitch distance ℓ^+ is varied in the present work between 10 and 40, five rows of solid inclusions are enough for the above-mentioned threshold of the substrate depth to be safely satisfied, for all the porous beds considered. The good agreement between the model results

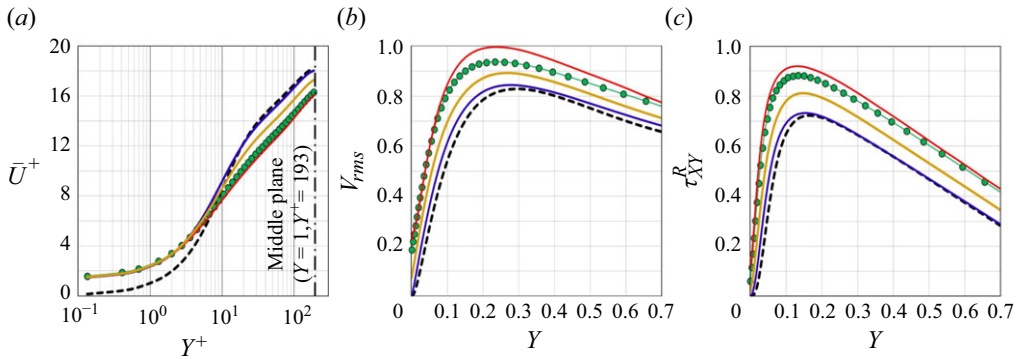


Figure 19. Turbulent channel flow ($Re_{\tau(\mathcal{M})} = 193$) over the porous substrate TC_{20} . Results of the fine-grained simulation (red lines) are used to validate the predictions of three different homogenized simulations, i.e. with the effective boundary conditions of the three velocity components imposed (green lines with filled circles), with the transpiration velocity suppressed (blue lines) or with the intrinsic medium permeability $\hat{\mathcal{K}}_{yy}$ set to zero in (2.21b) for the substrate to be modelled as a rough, impermeable wall (yellow lines). The dashed black profiles refer to the smooth, impermeable channel case.

and the grain-resolving simulation (§ 3.1) for the pattern TC_{20} (with bed depth ≈ 200 viscous units) confirm that this is the case. For the same configuration, we elaborate on the significance of incorporating the medium-permeability-related term in the transpiration velocity boundary condition (2.21b) by showing in figure 19 the predictions of the homogenization-based DNS when $\hat{\mathcal{K}}_{yy}$ is set to zero. It is clear that modelling such a deep porous substrate as a rough, impermeable boundary adversely affects the accuracy of the predictions, yet the results remain better than when transpiration at the fictitious interface is fully suppressed (the reader is also referred to the imposition of the transpiration velocity boundary condition, including the medium permeability effect, in the studies by Lācis *et al.* (2020) and Naqvi & Bottaro (2021), where different flow problems and porous patterns are considered). The role of the medium permeability is less important in the case of the patterns TM and LM for which $\mathcal{K}_{yy} \ll \mathcal{K}_{xy,zy}^{itf}$, as shown in table 1.

- (iv) Finally, for the case of shallow substrates (not treated here), one would probably need to define and solve different auxiliary, microscopic problems.

With respect to the applicability range of the effective boundary conditions (2.21a–2.21c), it is a complex undertaking to seek a single formal criterion that determines the limit of validity of the upscaling approach since the accuracy of the model can be sensitive to a large number of geometric and flow parameters, for instance, the size, shape and orientation of the grains, the porosity of the substrate, the degree of regularity of the surface microstructure and the Reynolds number. Taking all these factors into considerations requires extensive studies in which the model predictions are to be validated against fully resolving DNS and/or accurate experimental results. From a conceptual perspective, the first-order ‘Navier-slip’ effective conditions of the streamwise and the spanwise velocity components are valid only for vanishingly small surface elements, while taking the boundary conditions to higher order, including the definition of the transpiration velocity component (2.21b), allows us to consider larger surface manipulations. The incorporation of near-wall advection is believed to enhance significantly the robustness of the present model.

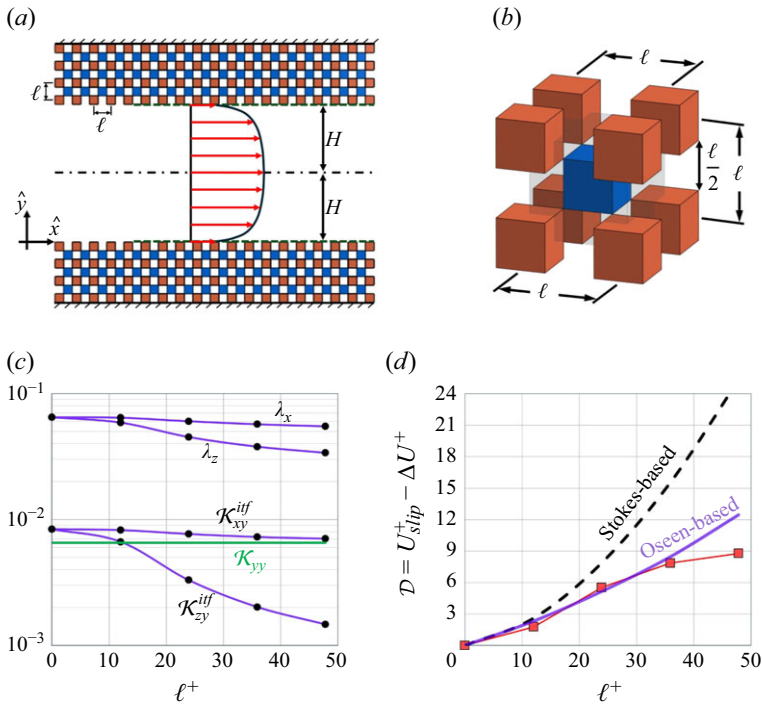


Figure 20. Turbulent flow in a symmetric channel bounded by permeable substrates consisting of staggered cubes: (a) sketch of the full domain considered by Hao & García-Mayoral (2025); (b) topology of the staggered pattern, where the unit cell dimensions are $\ell \times \ell \times \ell$; (c) the macroscopic coefficients, evaluated for different values of ℓ^+ following the procedure explained in § 2. Since the pattern is three-dimensional, we cannot set any of the spatial derivatives to zero to simplify closure problems (2.15) and (2.17). In (d) the behaviour of the parameter \mathcal{D} based on (3.12) with either the Oseen-based or the Stokes-based upscaled coefficients, validated against the reference results plotted with filled square symbols.

The discussion in § 3.3 highlights the role of the r.m.s. fluctuations of the transpiration velocity at the virtual plane, \tilde{V}_{rms} , key parameter that controls turbulence over irregular and porous walls; *ergo* we find it pertinent to judge, preliminarily, the applicability of the effective boundary conditions based on the level of \tilde{V}_{rms} estimated *a priori* from (3.11) as function of the macroscopic parameter Ψ of the rough/porous wall. The porous pattern chosen for validation of the homogenization-based model in § 3.1 is characterized by $\Psi \approx 5.4$ and \tilde{V}_{rms} close to 0.2; reasonable accuracy of the model is observed upon validation, which is encouraging taking into consideration the significantly low numerical cost of the homogenized DNS compared with the full texture-resolving ones.

Up to this point, only results for turbulence over anisotropic permeable substrates have been discussed, with the inclusions placed in an inline arrangement and infinitely elongated in either the streamwise (patterns *LC* and *LM*) or the spanwise (*TC* and *TM*) direction. It is appropriate, at this stage, to test the model also for the case of the turbulent flow over geometrically isotropic porous arrays consisting of three-dimensional staggered inclusions. This is more representative of patterns of packed grains. The configuration studied is illustrated in figure 20(a), one of those investigated via fine-grained numerical analysis by Hao & García-Mayoral (2025). The $\ell \times \ell \times \ell$ unit cell of the porous domain, shown in figure 20(b), consists of a full solid cube in the middle, with edge length $\ell/2$, and one-eighth of a cube at each of the corners, satisfying a porosity of 0.75. The Oseen-based

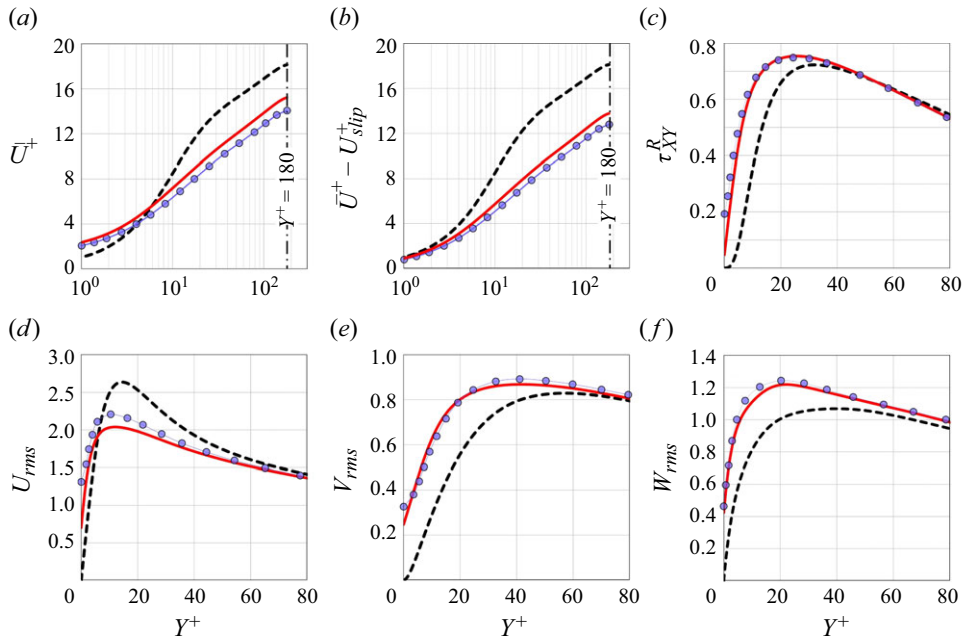


Figure 21. Distribution of the mean velocity and behaviours of sample turbulence statistics for the flow over staggered cubes characterized by $\theta = 0.75$ and $\ell^+ = 24$ (cf. figure 20): predictions of the homogenization-based DNS (red lines) are validated against results of the fine-grained DNS (filled circles) by Hao & García-Mayoral (2025), while the dashed profiles pertain to the smooth, impermeable channel case.

upscaled coefficients are evaluated for varying values of ℓ^+ (figure 20c), where the corresponding values of Ψ are estimated to be around (3.8, 6.3, 8.5, 10.7) when ℓ^+ is equal to (12, 24, 36, 48). While the values of the interface coefficients are close to those obtained earlier for the rough, impermeable surface (cf. figure 17), the corresponding values of Ψ are now larger due to the contribution of the medium permeability $\mathcal{K}_{yy} \approx 0.0065$ (cf. 3.10). Our predictions based on (3.12) for \mathcal{D} are calculated and plotted in figure 20(d); they match the reference results by Hao & García-Mayoral (2025) up to $\ell^+ \approx 36$ ($\Psi \approx 8.5$). Our DNS cannot extend up to such a value of Ψ , on account of the stability issues discussed in appendix A; running the model using the current computational scheme on cases for which \tilde{V}_{rms} exceeds 0.25 ($\Psi \gtrsim 6.5$) may result in questionable numerical solutions. A simulation, employing the effective boundary conditions is thus conducted for the same configuration shown in figure 20, with $\ell^+ \approx 24$ ($\Psi \approx 6.3$), near what we consider to be the limit of applicability of the model, defined with respect to the ability of the model to reproduce macroscopic feature-resolved results (e.g. roughness function, flow rate, skin friction coefficient, etc.) to within an approximation of $\pm 20\%$. For the pattern TC_{20} this occurs when $\Psi = 5.4$, as discussed in § 3.1. Sample results are displayed in figure 21 and are compared with those by Hao & García-Mayoral (2025). It is interesting that at such a value of Ψ the model can still provide trends reasonably consistent with the reference results, concerning the distribution of the mean streamwise velocity in the channel (which displays a considerable increase in drag) as well as the near-interface behaviours of the Reynolds stress and of the turbulent fluctuations in the velocity components. The present findings are encouraging for future research in which the accuracy of the model can be assessed (and adjustments/improvements of the formulation recommended) for several types of

wall microstructures, including irregular porous media and rough surfaces, ribletted walls, liquid-infused surfaces under the condition of lubricant depletion, etc.

5. Conclusions

Before summarizing the outcomes of the present work, it is useful to briefly outline the objectives we were planning to achieve. Our primary aim was to derive a model of wall boundary conditions capable to replace the expensive texture-resolving simulations of turbulent flows, to test its validity and assess its limitations. The boundary model derived extends that going by the name of Beavers–Joseph–Saffman in several respects: it goes to higher order in terms of the expansion parameter ϵ , it includes effects of advection (admittedly, in an approximate fashion) and it contains no empirical parameters. The second goal we were aiming to achieve was to find a correlation between the model constants (slip and permeability coefficients) and macroscopic features of the flow, such as the vertical fluctuating velocity and Hama's roughness function. The third objective was to assess whether the model's parameters, stemming from the microscopic simulations, could be used to make *a priori* predictions of turbulent flows in channels bounded by microstructured/permeable walls. We believe that, on all three counts above, several interesting advances have been made.

A more detailed account of results and conclusions now follows. The macroscopic parameters characterizing porous/rough walls are the two Navier–slip coefficients (λ_x , λ_z), the two interface permeability coefficients (\mathcal{K}_{xy}^{if} , \mathcal{K}_{zy}^{if}) and the intrinsic medium permeability (\mathcal{K}_{yy} , non-zero for sufficiently deep porous substrates); all of them are sensitive to both the microstructural details of the wall and to the level of advection in the vicinity of the interface. The asymptotic homogenization framework adopted incorporates the latter effect into the analysis of the microscale problem via an Oseen-like linearization, and a Reynolds number $Re_{slip} = \ell^+ U_{slip}^+$ hence appears in the closure problems used to evaluate the upscaled coefficients of the model, which contribute to the definition of high-order effective boundary conditions of the three velocity components (2.21a–2.21c) at a virtual plane boundary next to the physical porous/rough one.

The effective boundary conditions were employed to simplify a set of DNS of the turbulent flow in a channel delimited from one side (at $Y = 2$) by a smooth, impermeable wall and from the other side (at $Y \leq 0$) by a transversely isotropic porous substrate having a porosity $\theta = 0.5$. Four patterns of the substrate were studied, two streamwise-elongated and two spanwise-elongated, and for each of them four values of the inclusions pitch, ℓ^+ , were tested in the range $0 < \ell^+ < 40$. The model was validated, for one challenging case (transverse cylinders with $\ell^+ \approx 40$) against a fine-grained simulation, and acceptable agreement was found. The mean velocity profiles and the turbulence statistics at, and next to, the permeable walls were analysed to interpret the behaviour of the roughness function and the ensuing increase/reduction in skin-friction drag, ΔC_f %. Drag reduction (here up to 5 %) is achieved exclusively with substrates of streamwise-preferential permeability (where $\lambda_x^+ > \lambda_z^+$ and $\mathcal{K}_{xy}^{if,+} > \mathcal{K}_{zy}^{if,+}$), and is proportional, for small values of ℓ^+ , to $\Delta\lambda^+ = \lambda_x^+ - \lambda_z^+$. For the turbulent flow over substrates of spanwise-preferential permeability (or even those elongated in the streamwise direction and characterized by relatively large ℓ^+ values), an increase in the skin-friction drag is detected (here up to 27 %) and is accompanied by high levels of r.m.s. fluctuations in wall-normal and spanwise velocity components, in the Reynolds stress, τ_{xy}^R , and in the rate of production of turbulent kinetic energy, P_T , near the substrate/channel interface.

In view of the results extracted from the 16 DNS performed for the turbulent flow over modelled substrates, special attention was directed to the dependence of the roughness

function, ΔU^+ , on \tilde{V}_{rms} , \tilde{W}_{rms} and $\tilde{\tau}_{xy}^R$ (tildes are used to denote values at the porous–free-fluid interface, $Y = 0$). While the relation between ΔU^+ and each of these turbulence-characterizing quantities differs according to the geometry/configuration of the porous bed, the data are found to collapse quite well when specific roughness-function-related quantities are examined; they are $\mathcal{D} = U_{slip}^+ - \Delta U^+$ and $\mathcal{F} = \Delta \lambda^+ - \Delta U^+$, and they increase monotonically with \tilde{V}_{rms} , \tilde{W}_{rms} and $\tilde{\tau}_{xy}^R$. Moreover, evidence of the significant role played by \tilde{V}_{rms} as a control parameter in the turbulent flow over not only permeable but also rough, impermeable boundaries was demonstrated, particularly thanks to the work by Leonardi, Orlandi and collaborators (Leonardi *et al.* 2003; Orlandi & Leonardi 2006, 2008). The quantities \mathcal{D} and \mathcal{F} were expressed as functions of \tilde{V}_{rms} via the fitting correlations (3.3) and (3.6), respectively. To put these relationships to practical use in the *a priori* evaluation of the roughness function (i.e. without the need for running the DNS) the dependence of \tilde{V}_{rms} on the upscaled coefficients of the homogenization model was explored; based on the present results, a compound macroscopic quantity Ψ , defined by (3.10), is proposed as a single parameter correlated to \tilde{V}_{rms} . Eventually, the most significant result of the present study is the nexus found among the roughness function, the slip velocity and the upscaled coefficients, i.e.

$$\Delta U^+ = U_{slip}^+ - 11.5 \times (0.00075 \Psi^3 + 0.002 \Psi^2)^{0.6}, \tag{5.1}$$

$$\Delta U^+ = \Delta \lambda^+ - 11.5 \times (0.00075 \Psi^3 + 0.002 \Psi^2). \tag{5.2}$$

Although these equations are originally based on fitting the present results for the turbulent flow over porous substrates, they yield satisfactory agreement with simulation and experimental results for selected rough, impermeable boundaries (Hao & García-Mayoral 2025; Wong *et al.* 2024; Bechert *et al.* 1997), within the range of validity of the model (cf. § 4). One very interesting point is that the non-monotonic behaviour of ΔU^+ with the increase in ℓ^+ for the case of riblets (linear/nonlinear trends of drag reduction followed by performance degradation and eventually drag increase) can be captured by (5.2) up to ℓ^+ values of approximately 40.

The present analysis provides sufficient motivation to carry out further investigations for the purpose of either assessing the versatility of (5.1) and (5.2) for the turbulent flow over various textured boundaries or proposing more robust correlations. Once this is accomplished, the findings can be employed, for instance, to accelerate large-scale optimization studies of the wall microstructure (topology/size/arrangement of the grains), avoiding direct or large-eddy simulations at least in the preliminary stages of the work.

Supplementary movie. Supplementary movie is available at <https://doi.org/10.1017/jfm.2025.46>.

Funding. Activity funded by the European Union Next Generation EU, via PRIN PNRR 2022 grant, project code P2022CZ5KZ (‘SLIPS’).

Declaration of interests. The authors report no conflict of interest.

Appendix A. Considerations on the transpiration velocity boundary condition

The following assumptions/simplifications related to the imposition of the boundary condition (2.1*b*) in the DNS are adopted, mainly to guarantee the stability of the solution. Handling the pressure gradient $\partial \hat{p} / \partial \hat{y}$ at the fictitious plane $\hat{y} = 0$ is of much importance. If the physical wall were smooth and impermeable, one would write

$(\partial \hat{p} / \partial \hat{y})|_0 = \mu (\partial^2 \hat{v} / \partial \hat{y}^2)|_0$, which also applies to walls/substrates with small surface protrusions, e.g. vanishingly small values of ℓ^+ . The present work includes the study of the turbulent flow over porous substrates having relatively large values of ℓ^+ (up to ≈ 40), and thus the aforementioned expression becomes questionable. We have found it effective to incorporate the inertial effects associated with the transpiration velocity into the expression above, to obtain $(\partial \hat{p} / \partial \hat{y})|_0 = (\mu (\partial^2 \hat{v} / \partial \hat{y}^2) - \rho \hat{v} (\partial \hat{v} / \partial \hat{y}))|_0$. The boundary condition (2.21b) now reads

$$\hat{v}|_0 \approx \frac{\hat{K}_{yy}}{\mu} \left(\rho \hat{v} \frac{\partial \hat{v}}{\partial \hat{y}} + \mu \frac{\partial^2 \hat{v}}{\partial \hat{y}^2} \right) \Big|_0 - \hat{K}_{xy}^{itf} \frac{\partial}{\partial \hat{x}} \left(\frac{\partial \hat{u}}{\partial \hat{y}} + \frac{\partial \hat{v}}{\partial \hat{x}} \right) \Big|_0 - \hat{K}_{zy}^{itf} \frac{\partial}{\partial \hat{z}} \left(\frac{\partial \hat{w}}{\partial \hat{y}} + \frac{\partial \hat{v}}{\partial \hat{z}} \right) \Big|_0. \tag{A1}$$

With the continuity equation in mind, we have

$$\frac{\partial^2 \hat{v}}{\partial \hat{y}^2} \Big|_0 = \frac{\partial}{\partial \hat{y}} \left(\frac{\partial \hat{v}}{\partial \hat{y}} \right) \Big|_0 = \frac{\partial}{\partial \hat{y}} \left(-\frac{\partial \hat{u}}{\partial \hat{x}} - \frac{\partial \hat{w}}{\partial \hat{z}} \right) \Big|_0, \tag{A2}$$

and (A1) becomes

$$\begin{aligned} \hat{v}|_0 \approx & \hat{K}_{yy} \left(\frac{\rho}{\mu} \hat{v} \frac{\partial \hat{v}}{\partial \hat{y}} - \frac{\partial}{\partial \hat{x}} \frac{\partial \hat{u}}{\partial \hat{y}} - \frac{\partial}{\partial \hat{z}} \frac{\partial \hat{w}}{\partial \hat{y}} \right) \Big|_0 - \hat{K}_{xy}^{itf} \frac{\partial}{\partial \hat{x}} \left(\frac{\partial \hat{u}}{\partial \hat{y}} + \frac{\partial \hat{v}}{\partial \hat{x}} \right) \Big|_0 \\ & - \hat{K}_{zy}^{itf} \frac{\partial}{\partial \hat{z}} \left(\frac{\partial \hat{w}}{\partial \hat{y}} + \frac{\partial \hat{v}}{\partial \hat{z}} \right) \Big|_0. \end{aligned} \tag{A3}$$

Employing the Navier’s slip conditions

$$\hat{u}|_0 = \hat{\lambda}_x \left(\frac{\partial \hat{u}}{\partial \hat{y}} + \frac{\partial \hat{v}}{\partial \hat{x}} \right) \Big|_0 \approx \hat{\lambda}_x \frac{\partial \hat{u}}{\partial \hat{y}} \Big|_0, \quad \hat{w}|_0 = \hat{\lambda}_z \left(\frac{\partial \hat{w}}{\partial \hat{y}} + \frac{\partial \hat{v}}{\partial \hat{z}} \right) \Big|_0 \approx \hat{\lambda}_z \frac{\partial \hat{w}}{\partial \hat{y}} \Big|_0, \tag{A4}$$

to further simplify (A3), we eventually obtain the following expression:

$$\hat{v}|_0 \approx \frac{\rho \hat{K}_{yy}}{\mu} \left(\hat{v} \frac{\partial \hat{v}}{\partial \hat{y}} \right) \Big|_0 - \frac{\hat{K}_{xy}^{itf} + \hat{K}_{yy}}{\hat{\lambda}_x} \frac{\partial \hat{u}}{\partial \hat{x}} \Big|_0 - \frac{\hat{K}_{zy}^{itf} + \hat{K}_{yy}}{\hat{\lambda}_z} \frac{\partial \hat{w}}{\partial \hat{z}} \Big|_0. \tag{A5}$$

Note that the simplification made to the first-order Navier’s slip conditions in (A4) by neglecting the terms where \hat{v} appears derived with respect to either \hat{x} or \hat{z} relies on the fact that the vertical velocity at the wall is of order ϵ^2 (cf. 2.20b). This assumption is employed in particular to render $(\partial / \partial \hat{x}) (\partial \hat{u} / \partial \hat{y})|_0$ and $(\partial / \partial \hat{z}) (\partial \hat{w} / \partial \hat{y})|_0$ in the first term of (A3) equal to $(1 / \hat{\lambda}_x) (\partial \hat{u} / \partial \hat{x})|_0$ and $(1 / \hat{\lambda}_z) (\partial \hat{w} / \partial \hat{z})|_0$, respectively, while the complete first-order Navier’s slip conditions can be used directly for the interface-permeability-related terms. Interestingly, if the viscous terms $\mu (\partial^2 \hat{v} / \partial \hat{x}^2)|_0$ and $\mu (\partial^2 \hat{v} / \partial \hat{z}^2)|_0$ were included in the definition of $(\partial \hat{p} / \partial \hat{y})|_0$, the same expression (A5) would be obtained without the need for the approximation in (A4).

It is important to emphasize that any simplifications made here to the transpiration velocity boundary condition should be perceived as part of the modelling procedure, where our final validity criterion is the comparison between the results of the macroscopic model and the fine-grained DNS (cf. figures 6, 7 and 21). In this manner, we assess the combined influence of the different sources of errors entailed in the upscaling method on the accuracy of the predictions. For example, the transient term $-\rho (\partial \hat{v} / \partial t)|_0$, omitted here in the definition of $\partial \hat{p} / \partial \hat{y}|_0$, would contribute to $\hat{v}|_0$ by an amount $\hat{K}_{yy} (\rho / \mu) (\partial \hat{v} / \partial t)|_0$ which is of order $\epsilon^5 Re_\tau u_\tau$; this becomes as large as $\epsilon^2 u_\tau$, i.e. theoretically comparable

to the terms in (A5), when ϵ approaches 0.2 (for $Re_\tau \approx 190$). Nonetheless, one cannot quantify the inaccuracy of the method solely based on the growth of this term, unaccounted for in equation (A5). Ideally, should transient effects be significant in the microscopic region, a more sophisticated upscaling model would be needed to incorporate them, yielding macroscopic coefficients which are possibly time-variant (Zampogna *et al.* 2019b; Lasseux *et al.* 2019) and/or higher-order unsteady terms in the expressions of the effective boundary conditions (Ahmed *et al.* 2022a).

The following equation, which can be simply derived from (A5), is the expression of the transpiration velocity boundary condition implemented in the numerical code:

$$\hat{v}|_0 \approx \left(-\frac{\hat{\mathcal{K}}_{xy}^{itf} + \hat{\mathcal{K}}_{yy}}{\hat{\lambda}_x} \frac{\partial \hat{u}}{\partial \hat{x}} \Big|_0 - \frac{\hat{\mathcal{K}}_{zy}^{itf} + \hat{\mathcal{K}}_{yy}}{\hat{\lambda}_z} \frac{\partial \hat{w}}{\partial \hat{z}} \Big|_0 \right) / \left(1 - \frac{\rho \hat{\mathcal{K}}_{yy}}{\mu} \frac{\partial \hat{v}}{\partial \hat{y}} \Big|_0 \right). \quad (\text{A6})$$

Special attention is directed to the denominator of the right-hand-side term in (A6) since small values at one iteration may result in exceedingly large transpiration velocities, which can seriously disrupt the progress of the iterative process and the solution. For numerical calculations at a given time, \hat{t} , the value of the denominator is explicitly evaluated from the previous time instant, $\hat{t} - \Delta \hat{t}$. Clearly, for vanishingly small values of ℓ^+ , the near-interface advection is negligible compared with the viscous effects, and hence $(\rho \hat{\mathcal{K}}_{yy} / \mu) (\partial \hat{v} / \partial \hat{y})|_0$ approaches 0 so that the denominator in (A6) tends to 1. On the other hand, for porous substrates made of transverse/longitudinal cylindrical inclusions with the largest ℓ^+ studied here, the distributions of the value of the denominator over space (\hat{x} - \hat{z}) at different time instants are found to lie within a range extending from 0.25 to 2; values outside this range (recorded at less than 1% of the points on the virtual wall) are considered as outliers and are forced equal to the closest limit (either 0.25 or 2). Similarly, the value of the transpiration velocity $\hat{v}|_0$ is monitored and is bounded within $\pm 2 u_{\tau(\mathcal{M})}$, again with outliers detected at less than 1% of the points. It is worth noting that these outliers are observed here for the modelled substrates TC_{20} and LC_{20} only. If porous patterns with larger periodicity or porosity were considered, we would expect the errors associated with imposing such artificial limits to be more significant. Finally, for conservation of mass to be satisfied over the whole computational domain, the plane-averaged value of $\hat{v}|_0$ must vanish. Small deviations associated with numerical error are found to undermine convergence; to overcome this, the plane-averaged value of $\hat{v}|_0$ is evaluated every 10 time steps and uniformly subtracted from the local values.

At each time instant, evaluation of the effective boundary conditions takes place as part of the iterative process of the implicit scheme used for temporal discretization; the convergence of the numerical solution is demonstrated in figure 22 considering two sample cases, TC_{10} (figure 22a-c) and TC_{20} (figure 22d-f).

Appendix B. Normalization based on wall shear velocity

The macroscopic-pressure-gradient-based velocity scale $u_{\tau(\mathcal{M})}$ has been used for normalization throughout the paper. To facilitate comparisons with previous studies we also provide the values of the major parameters related to the mean velocity profile when normalized by the permeable-interface shear velocity $u_{\tau(\mathcal{B})}$, and of the model coefficients when $Re_{\tau(\mathcal{B})}$ is used in (3.2b) and (3.2c); these quantities are available in table 3. It is evident that the cases of skin-friction drag increase are characterized by shear-velocity ratios $u_{\tau(\mathcal{B})} / u_{\tau(\mathcal{M})}$, and therefore stress ratios $\tau_{\mathcal{B}} / \tau_{\mathcal{M}}$, larger than 1, which can be attributed to the fact that the shear stress at the permeable boundary for each of these cases, with account of the Reynolds stress, is larger than that at the top smooth wall. The

Substrate	$\frac{u_{\tau(B)}}{u_{\tau(M)}}$	λ_x^+	Macroscopic coefficients					Sample results		
			λ_z^+	$\mathcal{K}_{xy}^{if,+}$	$\mathcal{K}_{zy}^{if,+}$	\mathcal{K}_{yy}^+	U_{slip}^+	ΔU^+	$\Delta U_{ch}^+ \%$	$\Delta C_f \%$
Smooth	1	0	0	0	0	0	0	0	0	0
TC_5	1.008	0.43	0.65	0.20	0.49	0.17	0.43	-0.45	-1.8 %	+3.8 %
TC_{10}	1.023	0.81	1.17	0.71	1.64	0.71	0.81	-1.12	-5.4 %	+11.8 %
TC_{15}	1.037	1.10	1.52	1.29	2.76	1.65	1.10	-2.10	-9.7 %	+22.7 %
TC_{20}	1.068	1.38	1.83	1.99	3.98	3.10	1.35	-3.32	-16.0 %	+41.8 %
LC_5	0.996	0.66	0.43	0.51	0.21	0.17	0.67	+0.31	+1.5 %	-2.9 %
LC_{10}	0.996	1.32	0.87	2.06	0.83	0.68	1.34	+0.24	+1.3 %	-2.6 %
LC_{15}	1.011	2.01	1.32	4.77	1.92	1.57	2.03	-0.71	-2.5 %	+5.1 %
LC_{20}	1.045	2.78	1.82	9.05	3.65	2.97	2.75	-2.29	-10.8 %	+25.6 %
TM_5	1.014	0.55	1.04	0.36	1.05	0.01	0.55	-0.82	-3.6 %	+7.7 %
TM_{10}	1.037	0.98	1.78	1.10	3.29	0.05	0.98	-1.94	-8.9 %	+20.5 %
TM_{15}	1.063	1.30	2.22	1.83	5.47	0.11	1.28	-3.05	-14.5 %	+36.6 %
TM_{20}	1.078	1.55	2.49	2.45	7.31	0.21	1.49	-3.67	-17.7 %	+47.7 %
LM_5	0.990	1.08	0.56	1.11	0.38	0.01	1.08	+0.59	+2.9 %	-5.6 %
LM_{10}	0.988	2.15	1.12	4.41	1.49	0.04	2.18	+0.74	+3.8 %	-7.3 %
LM_{15}	1.010	3.30	1.72	10.38	3.52	0.10	3.32	-0.49	-1.4 %	+2.8 %
LM_{20}	1.024	4.47	2.33	18.96	6.42	0.19	4.38	-1.29	-5.2 %	+11.3 %

Table 3. Macroscopic coefficients and major results defined/normalized based on the fictitious-interface (bottom) shear velocity $u_{\tau(B)}$. The roughness function ΔU^+ is evaluated by averaging the shift in the mean streamwise velocity (taking the smooth channel case as a reference) over the region $30 \lesssim Y^+ \lesssim 120$, with Y^+ defined now based on $u_{\tau(B)}$.

Riblets' geometry	Dimensionless macroscopic coefficients			
	λ_x	λ_z	\mathcal{K}_{xy}^{if}	\mathcal{K}_{zy}^{if}
Equilateral triangle	0.1708	0.0807	0.02821	0.00586
Right triangle, symmetric	0.1397	0.0770	0.01683	0.00573
Right triangle, asymmetric	0.1273	0.0768	0.01411	0.00502
Trapezoidal	0.1915	0.0816	0.03484	0.00542
Thick blade	0.1144	0.0491	0.02102	0.00213
Thin blade	0.1915	0.0783	0.03788	0.00455

Table 4. Macroscopic coefficients for surfaces altered with riblets.

opposite applies to the cases of drag reduction. Accordingly, the values of ΔU^+ , $\Delta U_{ch}^+ \%$ and $\Delta C_f \%$ in table 3 are all larger, in absolute value, than those in table 2.

In figure 23, the values of $\mathcal{D} = U_{slip}^+ - \Delta U^+$ and $\mathcal{F} = \Delta \lambda^+ - \Delta U^+$ are plotted against Ψ (3.10), where the mean velocities and the macroscopic coefficients are normalized with either the macroscopic-pressure-gradient-based shear velocity $u_{\tau(M)}$ (cf. table 2) or the bottom-wall shear velocity, $u_{\tau(B)}$ (cf. table 3). For both choices of u_{τ} , the expressions (3.12) and (3.13) exhibit trends in reasonable agreement with the numerical results.

Appendix C. Macroscopic coefficients for surfaces with riblets

For the different ribletted surfaces sketched in figure 18, values of the upscaled coefficients contributing to the effective boundary conditions (2.20a–2.20c) are evaluated (table 4) for a virtual boundary at $\hat{y} = 0$, i.e. the plane passing through the tips/outer rims of the longitudinal protrusions. These walls are impermeable ($\mathcal{K}_{yy} = 0$), and they

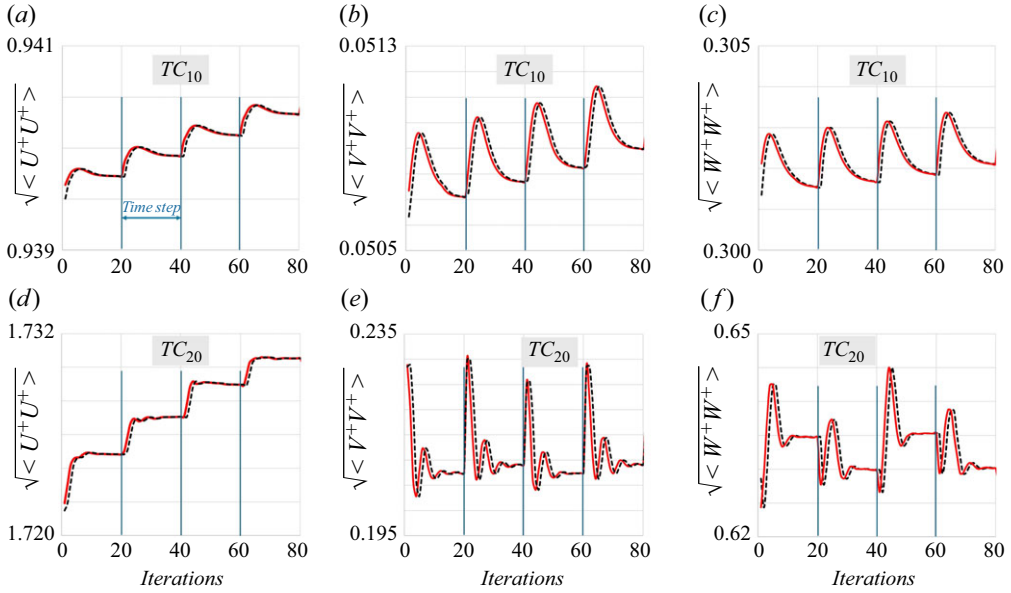


Figure 22. Convergence of $\sqrt{\langle U_i^+ U_i^+ \rangle}$ at $Y = 0$ during the iterative process, over four time steps (one time step requires 20 inner iterations of the implicit procedure; $\langle \rangle$ indicates $X - Z$ -spatial averaging). Red lines are plotted with the velocities obtained from the numerical solution at the end of each inner iteration, while black dashed lines are obtained by explicitly evaluating all terms in the effective conditions imposed in the code.

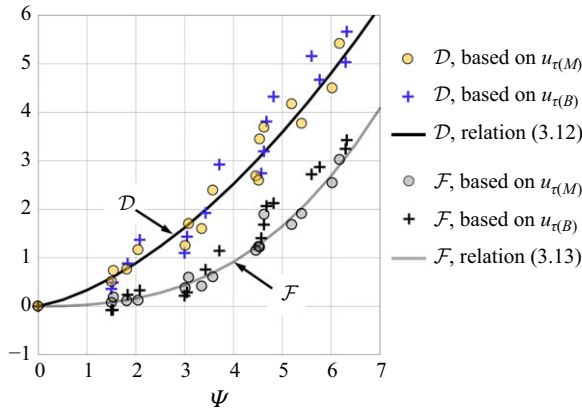


Figure 23. The quantities \mathcal{D} and \mathcal{F} plotted against the parameter Ψ for the 16 porous patterns modelled in this work. The results for these quantities are obtained with the parameters contributing to their definitions normalized based on either $u_{\tau(\mathcal{M})}$ or $u_{\tau(\mathcal{B})}$. Predictions of (3.12) and (3.13) are plotted with solid lines.

exhibit streamwise-preferential slip with $\lambda_x > \lambda_z$ and $\mathcal{K}_{xy}^{itf} > \mathcal{K}_{zy}^{itf}$. For each surface, the coefficients are calculated by solving the auxiliary systems (2.24) and (2.25) over a two-dimensional ($\hat{y} - \hat{z}$) elementary cell representative of the microscopic domain. The riblets are \hat{x} -elongated, which allows to set $\partial/\partial x_1$ to zero in the closure problems, thus rendering them advection-insensitive.

REFERENCES

- ABDERRAHAMAN-ELENA, N., FAIRHALL, C.T. & GARCÍA-MAYORAL, R. 2019 Modulation of near-wall turbulence in the transitionally rough regime. *J. Fluid Mech.* **865**, 1042–1071.
- ABDERRAHAMAN-ELENA, N. & GARCÍA-MAYORAL, R. 2017 Analysis of anisotropically permeable surfaces for turbulent drag reduction. *Phys. Rev. Fluids* **2** (11), 114609.
- AGNAOU, M., LASSEUX, D. & AHMADI, A. 2016 From steady to unsteady laminar flow in model porous structures: an investigation of the first Hopf bifurcation. *Comput. Fluids* **136**, 67–82.
- AHMED, E.N. & BOTTARO, A. 2024 Laminar flow in a channel bounded by porous/rough walls: revisiting Beavers-Joseph-Saffman. *Eur. J. Mech. B Fluids* **103**, 269–283.
- AHMED, E.N., BOTTARO, A. & TANDA, G. 2022a A homogenization approach for buoyancy-induced flows over micro-textured vertical surfaces. *J. Fluid Mech.* **941**, A53.
- AHMED, E.N., NAQVI, S.B., BUDA, L. & BOTTARO, A. 2022b A homogenization approach for turbulent channel flows over porous substrates: formulation and implementation of effective boundary conditions. *Fluids* **7** (5), 178.
- ANTONIA, R.A., ZHU, Y. & SOKOLOV, M. 1995 Effect of concentrated wall suction on a turbulent boundary layer. *Phys. Fluids* **7** (10), 2465–2474.
- BABUSKA, I. 1976 Homogenization and its application. Mathematical and computational problems. In *Numerical Solution of Partial Differential Equations—III*, (ed. HUBBARD, B.), pp. 89–116. Academic Press.
- BECHERT, D.W. & BARTENWERFER, M. 1989 The viscous flow on surfaces with longitudinal ribs. *J. Fluid Mech.* **206**, 105–129.
- BECHERT, D.W., BRUSE, M., HAGE, W., VAN DER HOEVEN, J.G.T. & HOPPE, G. 1997 Experiments on drag-reducing surfaces and their optimization with an adjustable geometry. *J. Fluid Mech.* **338**, 59–87.
- BERNARD, P.S., THOMAS, J.M. & HANDLER, R.A. 1993 Vortex dynamics and the production of reynolds stress. *J. Fluid Mech.* **253**, 385–419.
- BERNARDINI, M., GARCÍA CARTAGENA, E.J., MOHAMMADI, A., SMITS, A.J. & LEONARDI, S. 2021 Turbulent drag reduction over liquid-infused textured surfaces: effect of the interface dynamics. *J. Turbul.* **22** (11), 681–712.
- BOTTARO, A. 2019 Flow over natural or engineered surfaces: an adjoint homogenization perspective. *J. Fluid Mech.* **877**, P1.
- BOTTARO, A. & NAQVI, S.B. 2020 Effective boundary conditions at a rough wall: a high-order homogenization approach. *Meccanica* **55** (9), 1781–1800.
- BREUGEM, W.P., BOERSMA, B.J. & UITTENBOGAARD, R.E. 2006 The influence of wall permeability on turbulent channel flow. *J. Fluid Mech.* **562**, 35–72.
- BUDA, L. 2021 Drag reduction over rough permeable surfaces: a homogenized-based approach. Master's Thesis in Physics, University of Genoa, Italy.
- BURATTINI, P., LEONARDI, S., ORLANDI, P. & ANTONIA, R.A. 2008 Comparison between experiments and direct numerical simulations in a channel flow with roughness on one wall. *J. Fluid Mech.* **600**, 403–426.
- CHANG, J., JUNG, T., CHOI, H. & KIM, J. 2019 Predictions of the effective slip length and drag reduction with a lubricated micro-groove surface in a turbulent channel flow. *J. Fluid Mech.* **874**, 797–820.
- CHAVARIN, A., GÓMEZ-DE-SEGURA, G., GARCÍA-MAYORAL, R. & LUHAR, M. 2021 Resolvent-based predictions for turbulent flow over anisotropic permeable substrates. *J. Fluid Mech.* **913**, A24.
- CHENG, H. & CASTRO, I.P. 2002 Near wall flow over urban-like roughness. *Boundary-Layer Meteorol.* **104** (2), 229–259.
- CHENG, X.Q., WONG, C.W., HUSSAIN, F., SCHRÖDER, W. & ZHOU, Y. 2021 Flat plate drag reduction using plasma-generated streamwise vortices. *J. Fluid Mech.* **918**, A24.
- CHOI, K.S. 2002 Near-wall structure of turbulent boundary layer with spanwise-wall oscillation. *Phys. Fluids* **14** (7), 2530–2542.
- CHUNG, D., HUTCHINS, N., SCHULTZ, M.P. & FLACK, K.A. 2021 Predicting the drag of rough surfaces. *Annu. Rev. Fluid Mech.* **53** (1), 439–471.
- CLAUSER, F.H. 1954 Turbulent boundary layers in adverse pressure gradients. *J. Aeronaut. Sci.* **21** (2), 91–108.
- EL-SAMNI, O.A., CHUN, H.H. & YOON, H.S. 2007 Drag reduction of turbulent flow over thin rectangular riblets. *Intl. J. Engng Sci.* **45** (2-8), 436–454.
- ENDRIKAT, S., MODESTI, D., GARCÍA-MAYORAL, R., HUTCHINS, N. & CHUNG, D. 2021a Influence of riblet shapes on the occurrence of Kelvin–Helmholtz rollers. *J. Fluid Mech.* **913**, A37.
- ENDRIKAT, S., MODESTI, D., MACDONALD, M., GARCÍA-MAYORAL, R., HUTCHINS, N. & CHUNG, D. 2021b Direct numerical simulations of turbulent flow over various riblet shapes in minimal-span channels. *Flow Turbul. Combust.* **107** (1), 1–29.

- ESTEBAN, L.B., RODRÍGUEZ-LÓPEZ, E., FERREIRA, M.A. & GANAPATHISUBRAMANI, B. 2022 Mean flow of turbulent boundary layers over porous substrates. *Phys. Rev. Fluid* **7** (9), 094603.
- FAIRHALL, C.T., ABDERRAHAMAN-ELENA, N. & GARCÍA-MAYORAL, R. 2019 The effect of slip and surface texture on turbulence over superhydrophobic surfaces. *J. Fluid Mech.* **861**, 88–118.
- FLACK, K.A. & SCHULTZ, M.P. 2010 Review of hydraulic roughness scales in the fully rough regime. *ASME J. Fluids Engng* **132** (4), 041203.
- FLACK, K.A., SCHULTZ, M.P. & BARROS, J.M. 2020 Skin friction measurements of systematically-varied roughness: probing the role of roughness amplitude and skewness. *Flow Turbul. Combust.* **104** (2-3), 317–329.
- FLORES, O. & JIMÉNEZ, J. 2006 Effect of wall-boundary disturbances on turbulent channel flows. *J. Fluid Mech.* **566**, 357–376.
- FOROOGHI, P., STROH, A., MAGAGNATO, F., JAKIRLIĆ, S. & FROHNAPFEL, B. 2017 Toward a universal roughness correlation. *ASME J. Fluids Engng* **139** (12), 121201.
- FU, M.K., ARENAS, I., LEONARDI, S. & HULTMARK, M. 2017 Liquid-infused surfaces as a passive method of turbulent drag reduction. *J. Fluid Mech.* **824**, 688–700.
- GARCIA-MAYORAL, R. & JIMÉNEZ, J. 2011a Drag reduction by riblets. *Phil. Trans. R. Soc. Lond. A* **369** (1940), 1412–1427.
- GARCIA-MAYORAL, R. & JIMÉNEZ, J. 2011b Hydrodynamic stability and breakdown of the viscous regime over riblets. *J. Fluid Mech.* **678**, 317–347.
- GATTI, D., VON DEYN, L., FOROOGHI, P. & FROHNAPFEL, B. 2020 Do riblets exhibit fully rough behaviour? *Exp. Fluids* **61** (3), 81.
- GÓMEZ-DE-SEGURA, G. & GARCÍA-MAYORAL, R. 2019 Turbulent drag reduction by anisotropic permeable substrates—analysis and direct numerical simulations. *J. Fluid Mech.* **875**, 124–172.
- GÓMEZ-DE-SEGURA, G., SHARMA, A. & GARCÍA-MAYORAL, R. 2018a Turbulent drag reduction using anisotropic permeable substrates. *Flow Turbul. Combust.* **100** (4), 995–1014.
- GÓMEZ-DE-SEGURA, G., SHARMA, A. & GARCÍA-MAYORAL, R. 2018b Virtual origins in turbulent flows over complex surfaces. In *Center for Turbulence Research Proceedings of the Summer Program 2018* (ed. MOIN, P., & URZAY, J.) vol. 3, pp. 277–286. Stanford University.
- HAMA, F.R. 1954 Boundary layer characteristics for smooth and rough surfaces. *Trans. Soc. Nav. Archit. Mar. Engrs* **62**, 333–358.
- HAO, Z. & GARCÍA-MAYORAL, R. 2025 Turbulent flows over porous and rough substrates. *J. Fluid Mech.*, <https://doi.org/10.1017/jfm.2025.55>.
- IBRAHIM, J.I., GÓMEZ-DE-SEGURA, G., CHUNG, D. & GARCÍA-MAYORAL, R. 2021 The smooth-wall-like behaviour of turbulence over drag-altering surfaces: a unifying virtual-origin framework. *J. Fluid Mech.* **915**, A56.
- JEONG, J., HUSSAIN, F., SCHOPPA, W. & KIM, J. 1997 Coherent structures near the wall in a turbulent channel flow. *J. Fluid Mech.* **332**, 185–214.
- JIMÉNEZ BOLAÑOS, S. & VERNESCU, B. 2017 Derivation of the Navier slip and slip length for viscous flows over a rough boundary. *Phys. Fluids* **29** (5), 057103.
- JIMÉNEZ, J. 1994 On the structure and control of near wall turbulence. *Phys. Fluids* **6** (2), 944–953.
- JIMÉNEZ, J. 2004 Turbulent flows over rough walls. *Annu. Rev. Fluid Mech.* **36** (1), 173–196.
- JIMÉNEZ, J. & PINELLI, A. 1999 The autonomous cycle of near-wall turbulence. *J. Fluid Mech.* **389**, 335–359.
- JIMÉNEZ, J., UHLMANN, M., PINELLI, A. & KAWAHARA, G. 2001 Turbulent shear flow over active and passive porous surfaces. *J. Fluid Mech.* **442**, 89–117.
- JOUYBARI, M.A., YUAN, J., BRERETON, G.J. & MURILLO, M.S. 2021 Data-driven prediction of the equivalent sand-grain height in rough-wall turbulent flows. *J. Fluid Mech.* **912**, A8.
- KANG, S. & CHOI, H. 2000 Active wall motions for skin-friction drag reduction. *Phys. Fluids* **12** (12), 3301–3304.
- KHORASANI, S.M.H., LACIS, U., PASCHE, S., ROSTI, M.E. & BAGHERI, S. 2022 Near-wall turbulence alteration with the transpiration-resistance model. *J. Fluid Mech.* **942**, A45.
- KHORASANI, S.M.H., LUHAR, M. & BAGHERI, S. 2024 Turbulent flows over porous lattices: alteration of near-wall turbulence and pore-flow amplitude modulation. *J. Fluid Mech.* **984**, A63.
- KIM, J., MOIN, P. & MOSER, R. 1987 Turbulence statistics in fully developed channel flow at low Reynolds number. *J. Fluid Mech.* **177**, 133–166.
- KUWATA, Y. & SUGA, K. 2017 Direct numerical simulation of turbulence over anisotropic porous media. *J. Fluid Mech.* **831**, 41–71.
- LACIS, U., SUDHAKAR, Y., PASCHE, S. & BAGHERI, S. 2020 Transfer of mass and momentum at rough and porous surfaces. *J. Fluid Mech.* **884**, A21.

- LACIS, U., ZAMPOGNA, G.A. & BAGHERI, S. 2017 A computational continuum model of poroelastic beds. *Proc. R. Soc. Lond. A* **473** (2199), 20160932.
- LASSEUX, D., VALDÉS-PARADA, F.J. & BELLET, F. 2019 Macroscopic model for unsteady flow in porous media. *J. Fluid Mech.* **862**, 283–311.
- LEE, S., YANG, J., FOROOGHI, P., STROH, A. & BAGHERI, S. 2022 Predicting drag on rough surfaces by transfer learning of empirical correlations. *J. Fluid Mech.* **933**, A18.
- LEONARDI, S., ORLANDI, P., SMALLEY, R.J., DJENIDI, L. & ANTONIA, R.A. 2003 Direct numerical simulations of turbulent channel flow with transverse square bars on one wall. *J. Fluid Mech.* **491**, 229–238.
- LUCHINI, P. 1996 Reducing the turbulent skin friction. In *Computational Methods in Applied Sciences '96* (ed. DESIDERI, J.A.), pp. 466–470. Wiley.
- LUCHINI, P. 2015 The relevance of longitudinal and transverse protrusion heights for drag reduction by a superhydrophobic surface. In *European Drag Reduction and Flow Control Meeting – EDRFCM 2015*, pp. 81–82.
- LUCHINI, P., MANZO, F. & POZZI, A. 1991 Resistance of a grooved surface to parallel flow and cross-flow. *J. Fluid Mech.* **228**, 87–109.
- MANES, C., POGGI, D. & RIDOLFI, L. 2011 Turbulent boundary layers over permeable walls: scaling and near-wall structure. *J. Fluid Mech.* **687**, 141–170.
- MANSOUR, N.N., KIM, J. & MOIN, P. 1988 Reynolds-stress and dissipation-rate budgets in a turbulent channel flow. *J. Fluid Mech.* **194**, 15–44.
- MEI, C.C. & VERNESCU, B. 2010 *Homogenization Methods for Multiscale Mechanics*. World Science.
- MONTI, A., NICHOLAS, S., OMIDYEGANEH, M., PINELLI, A. & ROSTI, M.E. 2022 On the solidity parameter in canopy flows. *J. Fluid Mech.* **945**, A17.
- MORIMOTO, M., AOKI, R., KUWATA, Y. & SUGA, K. 2024 Measurements for characteristics of turbulence over a streamwise preferential porous substrate. *Flow Turbul. Combust.* **113** (1), 71–92.
- NAQVI, S.B. & BOTTARO, A. 2021 Interfacial conditions between a free-fluid region and a porous medium. *Intl J. Multiphase Flow* **141**, 103585.
- NAVIER, C. 1823 Mémoire sur les lois du mouvement des fluides. *Mém. Acad. R. Sci. Inst. France* **6**, 389–440.
- NIKURADSE, J. 1933 Laws of flow in rough pipes. NACA-TM-1292. Available at: <https://ntrs.nasa.gov/api/citations/19930093938/downloads/19930093938.pdf>.
- ORLANDI, P. & LEONARDI, S. 2006 DNS of turbulent channel flows with two- and three-dimensional roughness. *J. Turbul.* **7**, N73.
- ORLANDI, P. & LEONARDI, S. 2008 Direct numerical simulation of three-dimensional turbulent rough channels: parameterization and flow physics. *J. Fluid Mech.* **606**, 399–415.
- ORLANDI, P., LEONARDI, S. & ANTONIA, R.A. 2006 Turbulent channel flow with either transverse or longitudinal roughness elements on one wall. *J. Fluid Mech.* **561**, 279–305.
- ORLANDI, P., LEONARDI, S., TUZI, R. & ANTONIA, R.A. 2003 Direct numerical simulation of turbulent channel flow with wall velocity disturbances. *Phys. Fluids* **15** (12), 3587–3601.
- PARK, H., PARK, H. & KIM, J. 2013 A numerical study of the effects of superhydrophobic surface on skin-friction drag in turbulent channel flow. *Phys. Fluids* **25** (11), 110815.
- RASTEGARI, A. & AKHAVAN, R. 2015 On the mechanism of turbulent drag reduction with super-hydrophobic surfaces. *J. Fluid Mech.* **773**.
- ROSTI, M.E., BRANDT, L. & PINELLI, A. 2018 Turbulent channel flow over an anisotropic porous wall—drag increase and reduction. *J. Fluid Mech.* **842**, 381–394.
- ROSTI, M.E., CORTELEZZI, L. & QUADRIO, M. 2015 Direct numerical simulation of turbulent channel flow over porous walls. *J. Fluid Mech.* **784**, 396–442.
- SAFFMAN, P.G. 1971 On the boundary condition at the surface of a porous medium. *Stud. Appl. Math.* **50** (2), 93–101.
- SCHLICHTING, H. 1937 Experimental investigation of the problem of surface roughness. Washington, DC.: Natl. Adv. Comm. Aeronaut., Tech. Memo. 823.
- SHARMA, A. & GARCÍA-MAYORAL, R. 2020 Turbulent flows over dense filament canopies. *J. Fluid Mech.* **888**, A2.
- SHI, Z., KHORASANI, S.M.H., SHIN, H., YANG, J., LEE, S. & BAGHERI, S. 2024, Drag prediction of rough-wall turbulent flow using data-driven regression. arXiv: [2405.09256](https://arxiv.org/abs/2405.09256).
- SUDHAKAR, Y., LACIS, U., PASCHE, S. & BAGHERI, S. 2021 Higher-order homogenized boundary conditions for flows over rough and porous surfaces. *Transp. Porous Med.* **136** (1), 1–42.
- SUGA, K. 2016 Understanding and modelling turbulence over and inside porous media. *Flow Turbul. Combust.* **96** (3), 717–756.
- SUGA, K., OKAZAKI, Y., HO, U. & KUWATA, Y. 2018 Anisotropic wall permeability effects on turbulent channel flows. *J. Fluid Mech.* **855**, 983–1016.

- SUGA, K., TOMINAGA, S., MORI, M. & KANEDA, M. 2013 Turbulence characteristics in flows over solid and porous square ribs mounted on porous walls. *Flow Turbul. Combust.* **91** (1), 19–40.
- TOWNSEND, A.A. 1976 *The Structure of Turbulent Shear Flow*. 2nd edn. Cambridge University Press.
- VAN LEER, B. & NISHIKAWA, H. 2021 Towards the ultimate understanding of MUSCL: pitfalls in achieving third-order accuracy. *J. Comput. Phys.* **446**, 110640.
- VENKATAKRISHNAN, V. 1993 On the accuracy of limiters and convergence to steady state solutions. AIAA Meeting paper: 31st Aerospace Science Meeting, Reno, Nevada, USA, 11–14 January 1993. Available at: <https://doi.org/10.2514/6.1993-880>.
- VIJAY, S. & LUHAR, M. 2024 Pressure drop measurements over anisotropic porous substrates in channel flow. *Exp. Fluids* **65** (9), 135.
- VON DEYN, L.H., GATTI, D. & FROHNAPFEL, B. 2022 From drag-reducing riblets to drag-increasing ridges. *J. Fluid Mech.* **951**, A16.
- VREMAN, A.W. & KUERTEN, J.G.M. 2014 Comparison of direct numerical simulation databases of turbulent channel flow at $Re_\tau = 180$. *Phys. Fluids* **26** (1), 015102.
- WALLACE, J.M., ECKELMANN, H. & BRODKEY, R.S. 1972 The wall region in turbulent shear flow. *J. Fluid Mech.* **54** (1), 39–48.
- WALSH, M. & LINDEMANN, A. 1984 Optimization and application of riblets for turbulent drag reduction. AIAA Meeting paper: 22nd Aerospace Science Meeting, Reno, Nevada, USA, 9–12 January 1984. Available at: <https://doi.org/10.2514/6.1984-347>.
- WANG, W., CHU, X., LOZANO-DURÁN, A., HELMIG, R. & WEIGAND, B. 2021 Information transfer between turbulent boundary layers and porous media. *J. Fluid Mech.* **920**, A21.
- WANG, W., LOZANO-DURÁN, A., HELMIG, R. & CHU, X. 2022 Spatial and spectral characteristics of information flux between turbulent boundary layers and porous media. *J. Fluid Mech.* **949**, A16.
- WEST, A. & CARAENI, M. 2015 Jet noise prediction using a permeable FW-H solver. In *The 21st AIAA/CEAS Aeroacoustic Conference* Dallas, TX, USA, pp. 2371.
- WISE, D.J. & RICCO, P. 2014 Turbulent drag reduction through oscillating discs. *J. Fluid Mech.* **746**, 536–564.
- WONG, J., CAMOBRECO, C.J., GARCÍA-MAYORAL, R., HUTCHINS, N. & CHUNG, D. 2024 A viscous vortex model for predicting the drag reduction of riblet surfaces. *J. Fluid Mech.* **978**, A18.
- YANG, J., STROH, A., LEE, S., BAGHERI, S., FROHNAPFEL, B. & FOROOGHI, P. 2023 Prediction of equivalent sand-grain size and identification of drag-relevant scales of roughness – a data-driven approach. *J. Fluid Mech.* **975**, A34.
- YANG, J., STROH, A., LEE, S., BAGHERI, S., FROHNAPFEL, B. & FOROOGHI, P. 2024 Assessment of roughness characterization methods for data-driven predictions. *Flow Turbul. Combust.* **113** (2), 275–292.
- YANG, X.I.A. & MENEVEAU, C. 2016 Large eddy simulations and parameterisation of roughness element orientation and flow direction effects in rough wall boundary layers. *J. Turbul.* **17** (11), 1072–1085.
- YANG, X.I.A., SADIQUE, J., MITTAL, R. & MENEVEAU, C. 2016 Exponential roughness layer and analytical model for turbulent boundary layer flow over rectangular-prism roughness elements. *J. Fluid Mech.* **789**, 127–165.
- ZAMPOGNA, G., NAQVI, S.B., MAGNAUDET, J. & BOTTARO, A. 2019b Compliant riblets: problem formulation and effective macrostructural properties. *J. Fluids Struct.* **91**, 102708.
- ZAMPOGNA, G.A., MAGNAUDET, J. & BOTTARO, A. 2019a Generalized slip condition over rough surfaces. *J. Fluid Mech.* **858**, 407–436.